

Magnetic Amplification at Yb³⁺ "Designer Defects" in the van der Waals Ferromagnet, CrI₃

Kimo Pressler, Thom J. Snoeren, Kelly M. Walsh, Daniel R. Gamelin*

Department of Chemistry, University of Washington, Seattle, WA 98195, United States

Email: gamelin@uw.edu

Abstract. The two-dimensional (2D) van der Waals ferromagnet CrI₃ has been doped with the magnetic optical impurity Yb³⁺ to yield materials that display sharp multi-line Yb³⁺ photoluminescence (PL) controlled by the magnetism of CrI₃. Magneto-PL shows that Yb³⁺ magnetization is pinned to the magnetization of CrI₃. An effective internal field of ~10 T at Yb³⁺ is estimated, attributed to strong in-plane Yb³⁺-Cr³⁺ superexchange coupling. The anomalously low energy of Yb³⁺ PL in CrI₃ reflects relatively high Yb³⁺-I⁻ covalency, contributing to Yb³⁺-Cr³⁺ superexchange coupling. The Yb³⁺ PL energy and linewidth both reveal the effects of spontaneous zero-field CrI₃ magnetic ordering *within* 2D layers below T_C , despite the absence of net magnetization in multilayer samples. These results illustrate the use of optical impurities as "designer defects" to introduce unique functionality to 2D magnets.

Keywords: *2D Ferromagnet, Lanthanide Doping, Molecular Field, Chromium Triiodide, Photoluminescence*

Defects have the power to transform the physical properties of crystals, imparting new and potentially useful functionalities from conductivity to quantum photon emission.¹⁻⁶ In magnetic materials, defects can strongly affect spin-wave propagation, magnetic domain-wall propagation, skyrmion dynamics, and magnetic vortex pinning.⁷⁻⁹ Recently, the layered van der Waals ferromagnet CrI₃ has emerged as a promising platform for exploring strongly correlated spin physics, magnetic proximity effects, and next-generation spin-based device architectures in the

two-dimensional (2D) limit,¹⁰⁻¹⁴ but the potential to expand CrI₃ functionality through introduction of defects remains untapped. Here, we report that doping CrI₃ with Yb³⁺ as a "designer point defect" transforms its normally broad and featureless *d-d* photoluminescence (PL) into narrow-line sensitized *f-f* emission, without compromising its attractive magnetic properties. We further show that Yb³⁺ in CrI₃ experiences a large internal effective field that makes it extremely sensitive to small external magnetic fields. Using this property, we demonstrate magnetically saturated circular polarization of Yb³⁺ emission at anomalously small applied fields. Strikingly, the internal effective field also transmits magnetic information to Yb³⁺ even in the absence of any applied field, making Yb³⁺ a unique embedded luminescent probe of spontaneous zero-field magnetic ordering within the 2D monolayers of bulk CrI₃. These discoveries establish optical impurity doping as an effective strategy for expanding the functionality of 2D magnets, with potential ramifications for both basic science and future spin-phonic technologies.

CrI₃ has become a model system for exploring magnetic exchange in 2D van der Waals structures,¹⁰⁻¹⁴ stimulated by recent discoveries of Ising-like hard ferromagnetism in exfoliated monolayer CrI₃ and layer- and stacking-dependent magnetism in multi-layer CrI₃.^{15,16} Layering CrI₃ with non-magnetic 2D materials introduces magnetic functionality to the non-magnetic material *via* inter-layer exchange coupling, allowing magnetic manipulation of properties such as WSe₂ valley polarization and valley Zeeman splittings.¹⁷ Extension from few to many (bulk) layers preserves the strong Ising-like intralayer ferromagnetic ordering, but facile motion of domain walls unblocks demagnetization.¹⁸ Despite its rich magnetic properties, CrI₃ itself has not garnered much attention as an optical material. Bulk CrI₃ has been investigated for its very large Kerr and Faraday rotation strengths in relation to optical isolators and associated

technologies.^{19,20} PL of bulk CrI₃ has apparently not been reported, and few-layer CrI₃ shows¹⁷ only the very broad *d-d* PL characteristic of weak-field pseudo-octahedral Cr³⁺.²¹ Circular polarization of this *d-d* PL was used to probe the magnetism of few-layer CrI₃,¹⁷ but the emission's breadth limits its further utility for fundamental studies or in spin-photonics, stimulating efforts to narrow the band *via* cavity coupling.²² Doping CrI₃ with optically active impurities has also not been reported, either in bulk or exfoliated samples.

To investigate *intralayer* "proximity" effects resulting from magnetic exchange coupling, we have prepared CrI₃ doped with luminescent and spin-bearing Yb³⁺ ions. Large-diameter single-crystal flakes of CrI₃ were prepared by chemical vapor transport. Yb³⁺ was introduced by adding Yb(0) to the precursor mix. The Yb³⁺ concentration in the resulting Yb³⁺:CrI₃ crystals is controllable, and samples with up to ~5% Yb³⁺ (cation mole fraction, [Yb³⁺]/([Cr³⁺]+[Yb³⁺])) are described here. Further experimental details are provided in the Supporting Information (SI). Figure 1a shows a photograph of representative Yb³⁺:CrI₃ flakes in their growth tube. The flakes are between 5 and 10 mm across, with typical thicknesses of 5-20 μm (see SI). Figure 1b plots XRD data collected on undoped and 4.9% Yb³⁺-doped CrI₃ single-crystal flakes using a powder diffractometer. Only (00*l*) peaks are observed, corresponding to the interlayer lattice spacing and reflecting the flake's alignment. Figure 1c highlights the shift to smaller angle of the 001 peak upon doping. From fitting the XRD peak positions of undoped and 4.9% Yb³⁺-doped CrI₃ samples, the interlayer lattice parameter was found to increase 0.24% from 6.996 ± 0.002 to 7.013 ± 0.002 Å, attributed to the larger ionic radius of Yb³⁺ than Cr³⁺ (87 vs 62 pm, respectively) (see SI). These data suggest that the local strain of doping is relieved by distorting the lattice along its softest dimension, as expected. Substitutional incorporation of Yb³⁺ at the Cr³⁺ site is verified by single-crystal XRD measurements (see SI), which also show the increased

interlayer spacing. The single-crystal data show no detectable electron density between layers, ruling out Yb^{3+} intercalation.

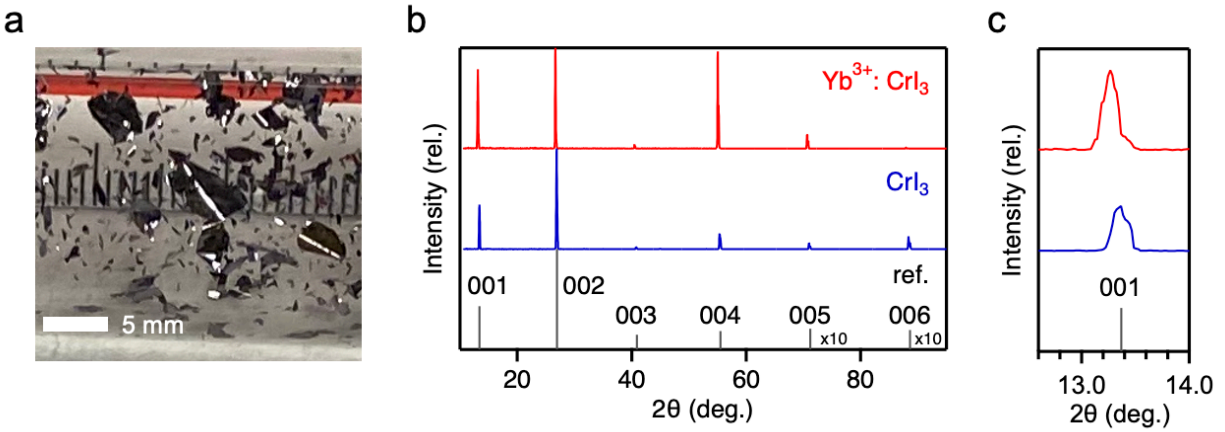


Figure 1. (a) Photograph of 4.9% $\text{Yb}^{3+}:\text{CrI}_3$ crystals prepared by chemical vapor transport. The scale bar shows 5 mm. All experiments were performed on individual single-crystal flakes from such a reaction tube. (b) XRD data collected on undoped and Yb^{3+} -doped CrI_3 single crystals using a powder diffractometer. Only $(00l)$ peaks are observed, indicating an oriented sample. Reference peaks for c -oriented CrI_3 diffraction are included (black, ICSD Coll. Code 251654). (c) Magnified view of the 001 reflection for the same samples, displaying an increase in the interlayer lattice spacing upon Yb^{3+} doping. The x axis in (c) was determined as described in the SI.

Figure 2a plots the PL spectra of CrI_3 and $\text{Yb}^{3+}:\text{CrI}_3$ single flakes measured at several temperatures between 4 and 200 K. The CrI_3 spectrum broadens and decreases in intensity with increasing temperature, eventually reaching only 7.5% of its 4 K intensity at 200 K (see SI). Although the broadening to higher energies is expected from thermal hot bands, the broadening to lower energies is abnormal and suggests an additional feature. Upon introduction of Yb^{3+} , the broad featureless $d-d$ emission of Cr^{3+} disappears and is replaced by a series of sharp $f-f$ transitions of Yb^{3+} around 1.15 eV. Assignment of the PL fine structure is discussed later. In some samples, Yb^{3+} doping also reveals another broad emission band centered at ~ 0.95 eV, which is responsible for the red tail of the CrI_3 PL here and in some literature spectra. This

feature has been traced to Ni^{2+} impurities (<0.4%) found in some Cr(0) precursors, and it can be mostly eliminated by using 5N Cr(0) precursors (Fig. 2a, bottom). The Yb^{3+} PL is not influenced by this Ni^{2+} impurity (see SI).

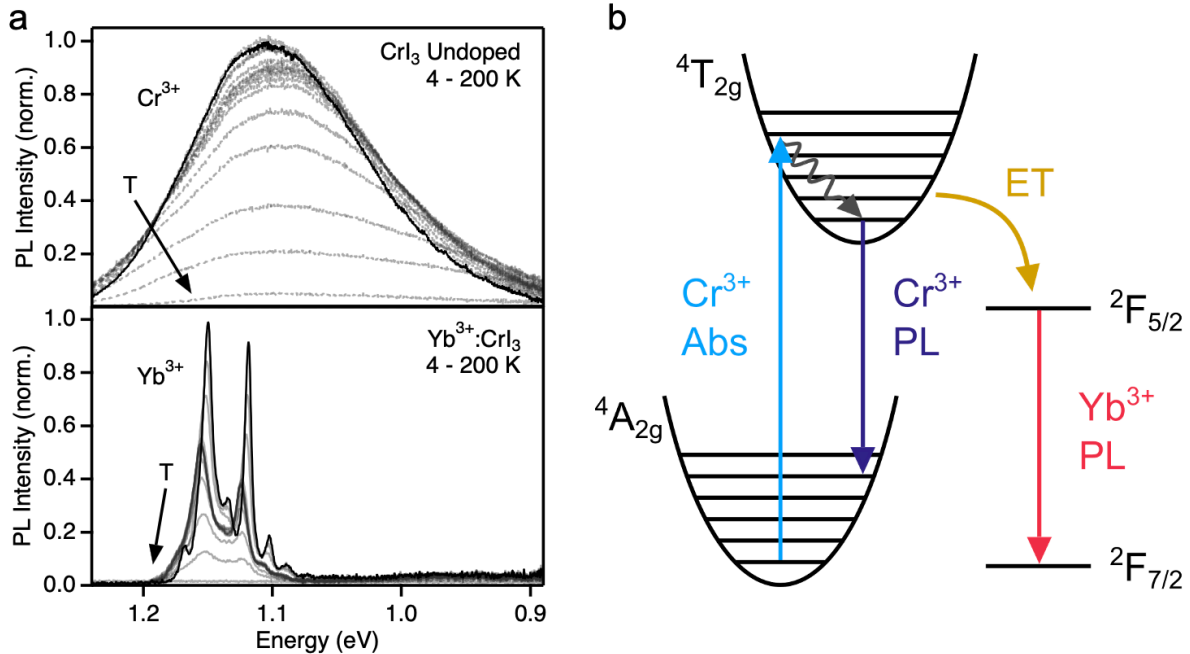


Figure 2. (a) Variable-temperature PL spectra of CrI_3 (top) and 4.9% $\text{Yb}^{3+}:\text{CrI}_3$ (bottom), measured from 4 to 200 K under 1.88 eV CW excitation at 4 mW/cm^2 . (b) Single-configurational-coordinate diagram (A_{1g} coordinate) describing vibronic broadening of the absorption and luminescence bands associated with transitions between the ${}^4A_{2g}$ and ${}^4T_{2g}$ ligand-field states of pseudo-octahedral Cr^{3+} . In Yb^{3+} -doped CrI_3 , energy transfer from the $\text{Cr}^{3+} {}^4T_{2g}$ excited state to Yb^{3+} yields sensitized ${}^2F_{5/2} \rightarrow {}^2F_{7/2}$ f - f luminescence.

Figure 2b illustrates the photophysics of $\text{Yb}^{3+}:\text{CrI}_3$ schematically. The lowest-energy excited state of CrI_3 is the $\text{Cr}^{3+} {}^4T_{2g}$ ligand-field state, involving excitation of a t_{2g} electron into a σ -antibonding e_g orbital (in idealized O_h symmetry). The resulting change in equilibrium geometry is described by the single-configurational-coordinate (SCC) diagram of Fig. 2b, which illustrates the totally symmetric distortion coordinate. This ${}^4T_{2g}$ excited state also distorts along a symmetry-breaking Jahn-Teller coordinate (not illustrated).²¹ These distortions lead to extensive

vibronic progressions in the absorption and PL spectra associated with this transition, and cause a large PL Stokes shift. Doping CrI₃ with Yb³⁺ introduces a set of ²F_{5/2} states just below the Cr³⁺ ⁴T_{2g} excited state, favorably positioned for efficient Cr³⁺ → Yb³⁺ energy transfer. At 4.9% Yb³⁺ doping, the Cr³⁺ ⁴T_{2g} PL is entirely quenched and strong Yb³⁺ ²F_{5/2} emission is observed in its place (Fig. 2a). Because both Cr³⁺ and Yb³⁺ states are localized at single ions, energy migration within the CrI₃ lattice is required for this complete quenching. In undoped CrI₃, energy migration among equivalent Cr³⁺ sites may occur but is not readily apparent. In Yb³⁺:CrI₃, this energy migration is interrupted when energy is captured by Yb³⁺ dopants. In 4.9% Yb³⁺:CrI₃, the average Cr³⁺ ion has only ~14% probability of having a neighboring Yb³⁺, and ~50% probability of having at least one Yb³⁺ within its first two cation shells. Energy must therefore migrate over at least a few lattice sites within the ⁴T_{2g} lifetime to fully quench the Cr³⁺ emission as observed in Fig. 2a.

Figure 3a shows the anticipated electronic structure of Yb³⁺ in CrI₃. In the free ion, spin-orbit coupling splits the ²F term into ²F_{5/2} (excited) and ²F_{7/2} (ground) states by an amount $\Delta E = 7/2\xi$, where $\xi = 361.8$ meV is the free-ion spin-orbit coupling constant.²³ In crystals, each of these states is further split by the crystal field. Figure 3b shows circularly polarized PL spectra of 4.9% Yb³⁺:CrI₃ measured in a 0.5 T field applied parallel to the crystal's *c* axis (*vide infra*). Three zero-phonon electronic origins are observed and assigned to the $\Gamma_8 \rightarrow \Gamma_6$, Γ_8 , and Γ_7 transitions anticipated from Fig. 3a using idealized *O_h* notation. The actual cation site symmetry in CrI₃ is lower (Fig. 3a, right),²⁴ but the expected low-symmetry splitting of the Γ_8 origin is not clearly identifiable. The Γ_6 peak is broad with observable structure on its high-energy shoulder, thus making the precise energy of this origin unclear within ~20 cm⁻¹ (~2.5 meV). Analysis of these PL energies within the Angular Overlap Model (AOM)²⁵ reproduces the ²F_{7/2} splittings well,

predicting a ${}^2F_{5/2}$ splitting of ~ 34 meV and splittings of the two Γ_8 levels by <0.5 meV each (see SI). Additional satellite features are observed ~ 127 cm^{-1} (15.7 meV) below the Γ_8 and Γ_7 electronic origins and assigned as phonon sidebands. Raman spectra show a totally symmetric lattice breathing mode of CrI_3 at this energy ($\nu = 127$ cm^{-1}).²⁶

A striking aspect of this $\text{Yb}^{3+}:\text{CrI}_3$ PL is its very low energy relative to other Yb^{3+} PL. This energy is primarily determined by spin-orbit coupling (Fig. 3a). Yb^{3+} spin-orbit coupling can be reduced from that in the free ion by covalent expansion of the f -electron wavefunctions (nephelauxetic effect),^{27,28} but f -orbital covalency in trivalent lanthanides is typically very small and this effect is usually considered negligible at ambient pressure. A survey of Yb^{3+} -doped crystals shows that the energy gap between $\text{Yb}^{3+} {}^2F_{5/2}$ and ${}^2F_{7/2}$ barycenters remains very near the free-ion value of $\Delta E \sim 1.266$ eV across doped oxide, fluoride, chloride, bromide, sulfide, and phosphide lattices (see SI).²⁹⁻³³ We note that we have been unable to find *any* reports of PL from other Yb^{3+} -doped iodide crystals, perhaps because Yb^{3+} is easily reduced to Yb^{2+} under common iodide crystal-growth conditions. $\text{Yb}^{3+}:\text{CrI}_3$ deviates from this typical behavior substantially: ΔE is only ~ 1.163 eV, or $\sim 9\%$ smaller than in the free ion, representing the smallest spin-orbit coupling yet reported for Yb^{3+} . Covalency in $\text{Yb}^{3+}:\text{CrI}_3$ is certainly enhanced by the large ionic radius and polarizability of the iodides, but this consideration alone likely cannot explain the anomaly. The atomic spin-orbit coupling of I is also much greater than those of other common ligands for Yb^{3+} , and should contribute to the spectroscopic spin-orbit splitting *via* covalency. Furthermore, the large ionic radius of Yb^{3+} compared to Cr^{3+} means that Yb^{3+} experiences an internal pressure imposed by the surrounding lattice, which may also increase covalency. Importantly, Yb^{3+} -I covalency is essential for strong Yb^{3+} - Cr^{3+} superexchange coupling.

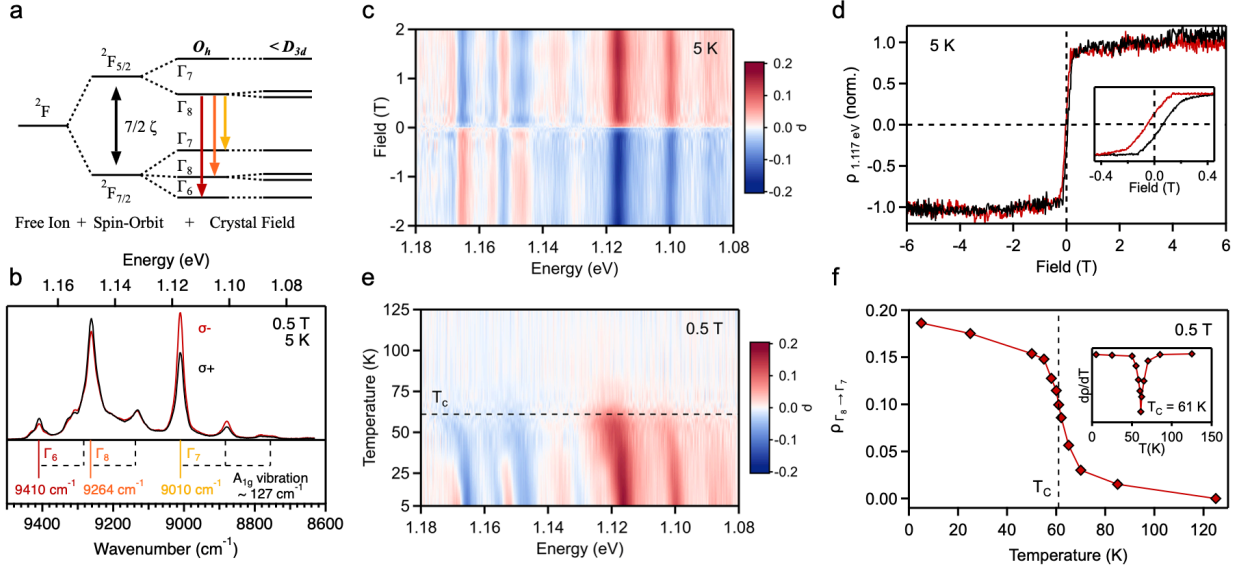


Figure 3. (a) Splitting of the Yb^{3+} free-ion 2F term due to spin-orbit (ζ) and crystal-field (O_h , $\langle D_{3d} \rangle$) interactions. The colored down arrows indicate the three crystal-field transitions anticipated in the low-temperature PL spectrum in the idealized O_h site symmetry. The actual site symmetry is reduced to $\langle D_{3d} \rangle$, e.g., to C_2 , splitting each Γ_8 level into two Kramers doublets. (b) Magnetic circularly polarized luminescence (MCPL) spectra of 4.9% $\text{Yb}^{3+}:\text{CrI}_3$ measured at 5 K with an applied magnetic field of 0.5 T. The σ^- (red) and σ^+ (black) spectra were collected using unpolarized 1.88 eV CW excitation at 40 mW/cm^2 and have different amplitudes. The three electronic origins in idealized O_h symmetry are indicated below the spectra, assigned to the $\Gamma_8 \rightarrow \Gamma_6$, Γ_8 , and Γ_7 transitions illustrated in panel (a). The dashed black lines indicate vibronic sidebands with a characteristic energy spacing of $\sim 127 \text{ cm}^{-1}$ (15.7 meV), consistent with the A_{1g} lattice mode of CrI_3 . (c) False-color plot of the MCPL polarization ratio, $\rho = (\sigma^- - \sigma^+)/(\sigma^- + \sigma^+)$, for the full Yb^{3+} PL spectrum, measured from -2 to +2 T at 5 K. (d) ρ of the $\Gamma_8 \rightarrow \Gamma_7$ electronic origin (1.117 eV) plotted as a function of magnetic field from -6 to 6 T. The black (red) trace corresponds to the positive (negative) field sweep direction. Inset: Expanded plot of ρ between -0.4 and +0.4 T, showing a coercive field of $\sim 55 \text{ mT}$. For both field-sweep measurements, the sample was excited with linearly polarized 1.96 eV excitation, but with different powers (see Methods). (e) False-color plot of the polarization ratio vs temperature, measured at 0.5 T. The dashed black line indicates the Curie temperature of bulk CrI_3 ($T_C = 61 \text{ K}$). (f) Plot of the $\Gamma_8 \rightarrow \Gamma_7$ polarization ratio at the peak maximum measured at 0.5 T as a function of temperature. The red curve is a guide to the eye. Inset:

Derivative of ρ as a function of temperature. The extracted Curie temperature is 61 K, indistinguishable from that of the undoped crystal.

From Fig. 3a, all features show circularly polarized PL, with the $\Gamma_8 \rightarrow \Gamma_7$ origin showing the greatest polarization ratio ($\rho = (\sigma^- - \sigma^+)/(\sigma^- + \sigma^+) = 19\%$). ρ is independent of excitation power but its maximum value varies somewhat between samples (see SI). Figure 3c plots ρ across the entire PL spectrum as a function of magnetic field. All Yb^{3+} transitions are influenced by the applied field in the same way, consistent with all PL arising from the same excited state (Γ_8). Figure 3d plots ρ for the $\Gamma_8 \rightarrow \Gamma_7$ peak as a function of applied field. ρ increases rapidly at very low fields and saturates at only ~ 0.2 T. Increasing the field from 0.2 to 6.0 T does not change ρ further, consistent with complete magnetization of Yb^{3+} by 0.2 T. On an expanded scale, these data show a hysteresis with coercivity of ~ 55 mT, comparable to that found in magnetic measurements of bulk CrI_3 .^{18,34} We note that these ρ values are generally small compared to those in cubic $\text{Yb}^{3+}:\text{InP}$ ($\sim 70\%$ at 10 T, 4.2 K),³³ possibly suggesting an in-plane or canted Yb^{3+} anisotropy. Figure 3e summarizes the temperature dependence of ρ , measured at 0.5 T, and Fig. 3f highlights the temperature dependence for $\Gamma_8 \rightarrow \Gamma_7$ individually. All spectral features behave similarly, showing a pronounced drop in polarization at the Curie temperature of bulk CrI_3 (~ 61 K, see Fig. 3f, inset). These magneto-optical data agree well with magnetic susceptibility data (see SI), and both indicate that Yb^{3+} doping causes no significant change in the magnetic characteristics of CrI_3 in these samples. This MCPL field and temperature dependence is highly unusual for Yb^{3+} , which generally shows simple paramagnetism of a pseudo-spin 1/2. For example, our AOM crystal-field analysis (see SI) predicts $g_{\text{avg}} \sim 2.7$ for the lowest ${}^2F_{7/2}$ Kramers doublet. Overall, the anomalous magnetism seen in the Yb^{3+} MCPL reflects *magnetic* integration of Yb^{3+} with ferromagnetic CrI_3 .

Magnetic ordering was originally explained by Weiss in terms of a huge internal "molecular field"³⁵ exerted upon individual ions by their surrounding magnetic matrix, and this model provides a useful heuristic for estimating the effective field experienced by Yb^{3+} within CrI_3 . In this model, the effective field is given by the sum of external and molecular fields, as in eq 1.

$$H_{\text{eff}} = H_{\text{ext}} + H_{\text{mol}} \quad (1)$$

In Fig. 3c,d, CrI_3 reaches magnetic saturation at very small H_{ext} (<0.2 T). At such low fields, $H_{\text{ext}} \ll H_{\text{mol}}$, and hence $H_{\text{eff}} \sim H_{\text{mol}}$. In the molecular-field model, H_{mol} in CrI_3 is given by eq 2,

$$H_{\text{mol}} = \frac{2zJ\langle S \rangle}{g\mu_B} \quad (2)$$

where, J is the nearest-neighbor exchange coupling constant, $z = 3$ in CrI_3 , g is the Landé g factor (2.00 for Cr^{3+} in CrI_3), μ_B is the Bohr magneton, and $\langle S \rangle$ is the spin expectation value for Cr^{3+} in CrI_3 , whose absolute value equals $3/2$ at saturation. T_C in this model is determined by J according to eq 3,

$$T_C = \frac{2zJS(S+1)}{3k_B} \quad (3)$$

where $S = 3/2$ for Cr^{3+} , and k_B is the Boltzmann constant. From $T_C = 61$ K, eq 3 yields a value of $J = 0.70$ meV in CrI_3 . Entering this J value into eq 2 yields $H_{\text{mol}} = \sim 54$ T in CrI_3 . H_{mol} is dominated by superexchange coupling, since dipolar contributions cannot account for the high T_C of CrI_3 .³⁶ For Yb^{3+} in CrI_3 , J is reduced by the shielding of the $4f$ orbitals. $\text{Cr}^{3+}(d)$ - $\text{Yb}^{3+}(f)$ superexchange coupling has received relatively little experimental or theoretical attention,³⁷⁻³⁹ but relevant experimental data are found in inelastic neutron scattering analyses of $\text{Cs}_3\text{Yb}_{1.8}\text{Cr}_{0.2}\text{Br}_9$, where Yb^{3+} - Cr^{3+} exchange splittings are $\sim 1/4$ those for Cr^{3+} - Cr^{3+} .³⁷ This scaling factor is approximate because of the different lattice structure, but $\text{Cs}_3\text{Yb}_{1.8}\text{Cr}_{0.2}\text{Br}_9$ is the most similar halide-bridged Yb^{3+} - Cr^{3+} system for which reliable exchange-coupling strengths could be found. This rough scaling reduces H_{mol} to ~ 14 T. Accounting for the larger g value of

Yb^{3+} (~ 2.7 , see SI), our best estimate is $H_{\text{mol}} \sim 10$ T for Yb^{3+} ions within CrI_3 . Future spectroscopic measurements (*e.g.*, inelastic neutron scattering, Mössbauer, *etc.*) and calculations will be needed to refine this estimate, but the central conclusion drawn from both the experimental data and this analysis is clear: Yb^{3+} magnetization in $\text{Yb}^{3+}:\text{CrI}_3$ is effectively pinned to the magnetic ordering of the CrI_3 lattice through strong $\text{Yb}^{3+}\text{-Cr}^{3+}$ superexchange coupling. The large H_{mol} in $\text{Yb}^{3+}:\text{CrI}_3$ is attributable in large part to the $\text{Yb}^{3+}\text{-I}$ covalency discussed above. For comparison, exchange fields of 1.7 and ~ 1.1 T are reported for Yb^{3+} in ferrimagnetic hexagonal YbFeO_3 ⁴⁰ and distorted orthorhombic YbCrO_3 .⁴¹ At these values, Yb^{3+} magnetization is not pinned to the ordered TM^{3+} spin sublattices.

A further remarkable aspect of $\text{Yb}^{3+}:\text{CrI}_3$ is that the effects of H_{mol} are evident even at zero magnetic field ($H_{\text{ext}} = 0$). Figure 4a plots zero-field Yb^{3+} PL spectra as a function of temperature from 4 to 200 K. Viewing the data starting from high temperature, the peak positions appear nearly constant until roughly T_C . Below T_C , the peaks all shift to lower energy together. This redshift is also evident in Fig. 3e. Figure 4b highlights the temperature dependence of the $\Gamma_8 \rightarrow \Gamma_7$ transition energy. From 120 K to $\sim T_C$, the transition energy increases gradually by only ~ 2 meV. Such temperature dependence has been variously modeled in terms of Raman scattering of non-resonant phonons or direct absorption/emission of phonons resonant with a crystal-field splitting.^{42,43} For example, both models reproduce the ${}^2\text{F}_{7/2} \rightarrow {}^2\text{F}_{5/2}$ transition energies of $\text{Yb}^{3+}:\text{YAG}$ well, whereas the resonant phonon model reproduces absorption linewidths marginally better.⁴³ As such, we apply the resonant phonon model here. The PL energies above T_C are thus described by eq 4,^{42,43}

$$E(T) = E_0 + \frac{\alpha_s}{e^{\Delta/k_B T} - 1} \quad T > T_C \quad (4)$$

where E_0 is the energy at 0 K, α_s describes the electron-phonon interaction strength, and Δ is the energy of the activating phonon mode, fixed at $\Delta = 127 \text{ cm}^{-1}$ (15.7 meV, Fig. 3b).

The solid curve in the high-temperature portion of Fig. 4b ($>T_C$) shows a fit to the high-temperature data using eq 4, floating E_0 and α_s and yielding best-fit values of 1.1242 eV and -6.3 meV, respectively. Eq 4 plateaus at E_0 in the limit of 0 K (dashed line $< T_C$ in Fig. 4b), but the experimental peak energy shows a discontinuity at T_C , dropping sharply and decreasing with decreasing temperature until reaching ~ 7 meV below E_0 in the low-temperature limit. With its link to T_C and its characteristic curvature, this trend in Yb^{3+} PL energy is associated with the spontaneous magnetization of individual CrI_3 monolayers, even though there is no net magnetization in these samples.

Spontaneous ferromagnetic ordering is classified as a second-order phase transition and, within the theory of universal scaling laws, is characterized by the order parameter β shown in eq 5 describing the magnetization temperature dependence.⁴⁴

$$M(T) = M_0 \left(-\frac{T-T_C}{T_C} \right)^\beta \quad (5)$$

M_0 is the saturation moment per magnetic ion and equals $3.1 \mu_B$ for CrI_3 .¹⁸ The precise value of β depends on the underlying spin physics, but it is commonly around $1/3$.¹² Previous examination of bulk CrI_3 found a critical exponent of $\beta = 0.284$, between that expected from the 3D Ising model ($\beta = 0.325$) and that of the tri-critical mean-field model ($\beta = 0.250$).³⁴ Accordingly, the data in Fig. 4b below T_C were simulated using eq 6 (sum of eq 4 and eq 5, with eq 4 parameters fixed by the high-temperature data). The scaling parameter (γ) in eq 6 relates magnetization to PL energy shift. The data are reproduced well using fixed values of $\beta = 1/3$, $T_C = 60$ K, and $\Delta = 127 \text{ cm}^{-1}$ (15.7 meV), with γ as the only adjustable parameter. Relating eqs 5 and 6, these results indicate an Yb^{3+} PL energy shift of $-2.2 \text{ meV}/\mu_B$ during spontaneous CrI_3 intralayer

magnetization. We stress that the zero-field PL data in Fig. 4 are not magnetic data, but highlight the strong influence of CrI₃ spontaneous magnetization on the Yb³⁺ PL. Because T_C in these samples is indistinguishable from that of bulk CrI₃ (Figs. 3f, S15), we tentatively attribute the small apparent broadening of the PL energy discontinuity around T_C in Fig. 4b to additional PL hot bands that are not spectrally resolved.

$$E(T) = E_0 + \frac{\alpha_s}{e^{\Delta/k_B T} - 1} + \gamma \left(-\frac{T - T_C}{T_C} \right)^\beta \quad T < T_C \quad (6)$$

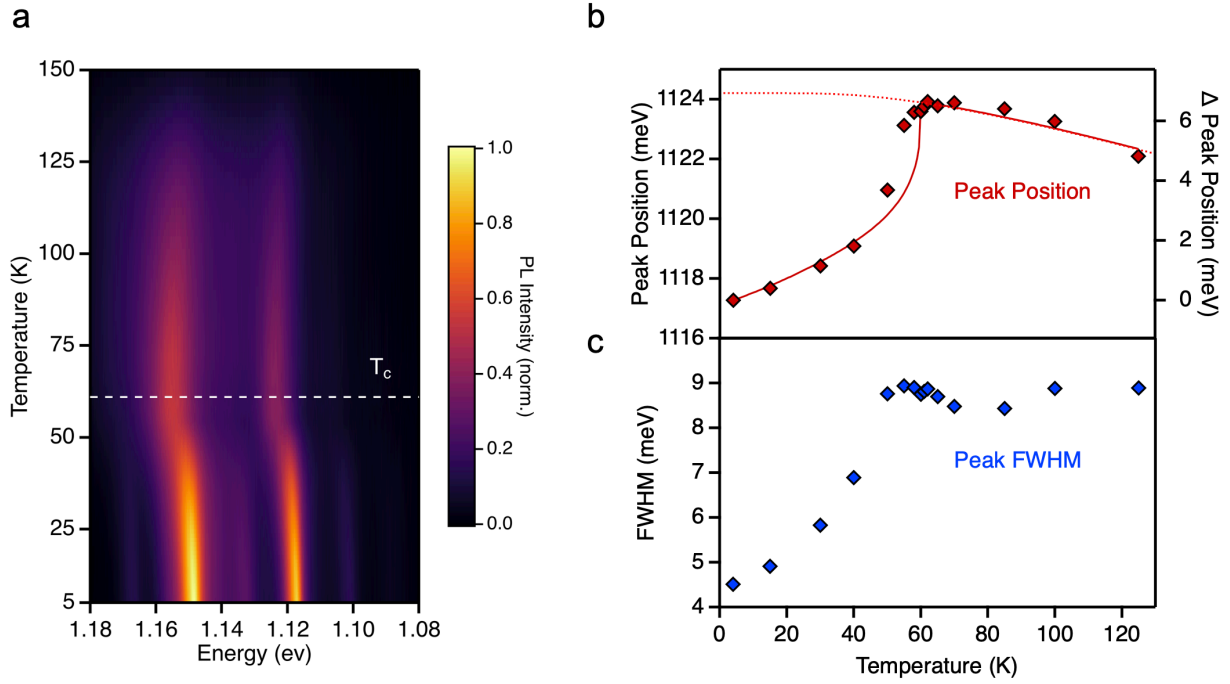


Figure 4. (a) False-color plot of the Yb³⁺ PL intensities vs temperature measured for 4.9% Yb³⁺:CrI₃ from 4 to 150 K at zero external magnetic field. The horizontal dashed line indicates $T_C = 61$ K. (b) Peak position of the $\Gamma_8 \rightarrow \Gamma_7$ transition plotted vs temperature. The solid red curve shows the behavior predicted from the combination of resonant phonon interactions (eq 4) and spontaneous magnetization (below T_C , eq 6). The dashed red curve shows the behavior predicted from eq 4 alone below T_C . The solid curve was obtained using eqs 4 and 6 with fixed parameters of $\Delta = 127$ cm⁻¹ (15.7 meV), $T_C = 60$ K, and $\beta = 1/3$, adjusting only the amplitude scaling. (c) Plot of the $\Gamma_8 \rightarrow \Gamma_7$ PL linewidth vs temperature, from the same VTPL measurements.

Figure 4c plots the temperature dependence of the $\Gamma_8 \rightarrow \Gamma_7$ linewidth (full-width-at-half-maximum, FWHM). These data show similar trends as observed in the peak energies of Fig. 4b. Below T_C , the FWHM decreases from ~ 9 meV to ~ 4.5 meV in the low-temperature limit, attributed to the reduction in spin disorder around Yb^{3+} . These data thus also reflect spontaneous magnetic ordering in monolayers of CrI_3 . Although distinct low-energy shoulders are not resolved in these data, we hypothesize that the energy and linewidth changes below T_C both ultimately stem from loss of hot-magnon sideband intensity as CrI_3 monolayers order magnetically.⁴⁵ It will be an interesting future direction to explore magnon coupling to f - f transitions in these and related doped 2D magnetic materials.

In summary, doping Yb^{3+} into the 2D van der Waals ferromagnet CrI_3 transforms this material's PL from broad-band to sharp multi-line, while retaining its key magnetic functionality. The f - f PL of $\text{Yb}^{3+}:\text{CrI}_3$ is anomalously low in energy, reflecting relatively covalent Yb^{3+} -I bonding. Yb^{3+} magnetization is pinned to CrI_3 by strong superexchange interactions, which contribute an effective internal field of ~ 10 T that is greater than the field required for magnetic saturation of paramagnetic Yb^{3+} and much greater than the field required for full CrI_3 magnetization at low temperature (~ 0.2 T). Flipping the magnetization of CrI_3 with a small external field thus also flips the Yb^{3+} magnetization and inverts its PL circular polarization. Magnetic pinning is maintained up to the T_C of CrI_3 , but is rapidly lost above T_C . We further showed that the Yb^{3+} PL energy and linewidth both sense this internal field even at zero applied field, mapping spontaneous *intralayer* magnetic ordering below T_C despite the absence of net magnetization. Because each Yb^{3+} ion is a local lattice defect within an individual CrI_3 monolayer, we expect these induced functionalities to persist down to the monolayer, prompting future studies on exfoliated $\text{Yb}^{3+}:\text{CrI}_3$ and associated stacked van der Waals heterostructures and

layered devices. These results demonstrate the power of designer defects to add functionality to 2D magnetic materials, enrich their fundamental physics, and create new materials of potential utility for future spin-photonics applications.

Acknowledgments. Support of this project by the US NSF (DMR-1807394) is gratefully acknowledged. Initial stages of this work were performed as part of Programmable Quantum Materials, an Energy Frontier Research Center funded by the U.S. Department of Energy (DOE), Office of Science, Basic Energy Sciences (BES), under award DESC0019443. Additional support was received from the UW Clean Energy Institute (graduate fellowships to T.J.S. and K.M.W.). Part of this work was conducted at the Molecular Analysis Facility, a National Nanotechnology Coordinated Infrastructure (NNCI) site at the University of Washington that is supported in part by the National Science Foundation (NNCI-1542101 and NNCI-2025489), the University of Washington, the Molecular Engineering & Sciences Institute, the Clean Energy Institute, and the National Institutes of Health. The authors thank Dr. Werner Kaminsky and Paige M. Gannon for single-crystal XRD measurements, Dr. Xi Wang for assistance with optical microscope measurements, Prof. Jiun-Haw Chu and Dr. Zhaoyu Liu for VSM measurements, and Prof. Robert Glaum, Maximilian Jähnig, and Julia Spitz for provision of and assistance with the BonnMag code.

Author Information

Corresponding Author

Daniel R. Gamelin - *Department of Chemistry, University of Washington, Seattle, Washington 98195-1700, United States*; orcid.org/0000-0003-2888-9916;

Email: gamelin@chem.washington.edu

Authors

Kimo Pressler - *Department of Chemistry, University of Washington, Seattle, Washington 98195-1700, United States*; orcid.org/0000-0003-2788-1592

Thom J. Snoeren - *Department of Chemistry, University of Washington, Seattle, Washington 98195-1700, United States*; orcid.org/0000-0001-8055-3710

Kelly M. Walsh - *Department of Chemistry, University of Washington, Seattle, Washington 98195-1700, United States*; orcid.org/0000-0001-5349-8816

Supporting Information

The Supporting Information is available free of charge at <https://pubs.acs.org/doi/XXXX>

Additional experimental details, including about sample preparation and characterization. Additional variable-temperature PL data, PL polarization vs magnetic field data, excitation-power-dependence data, results from Yb³⁺ crystal-field calculations, and comparison of Yb³⁺ crystal-field barycenter energies in various lattices (PDF).

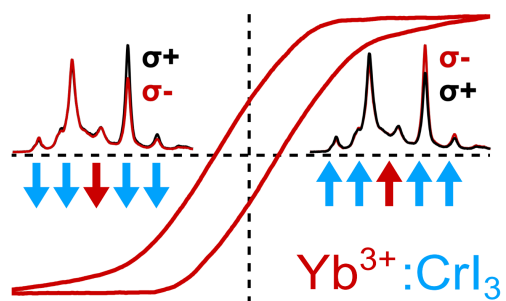
References

- (1) Cox, P. A., *Electronic Structure and Chemistry of Solids*. Oxford University Press: Oxford, 1987.
- (2) Henderson, B.; Imbusch, G. F., *Optical Spectroscopy of Inorganic Solids*. Oxford University Press: Oxford, 1989.
- (3) Kittel, C., *Introduction to Solid State Physics*. 8 ed.; Wiley: New York, 2004.
- (4) Bassett, L. C.; Alkauskas, A.; Exarhos, A. L.; Fu, K.-M. C., Quantum defects by design. *Nanophotonics* **2019**, *8*, 1867-1888.
- (5) Tran, T. T.; Elbadawi, C.; Totonjian, D.; Lobo, C. J.; Grosso, G.; Moon, H.; Englund, D. R.; Ford, M. J.; Aharonovich, I.; Toth, M., Robust Multicolor Single Photon Emission from Point Defects in Hexagonal Boron Nitride. *ACS Nano* **2016**, *10*, 7331-7338.
- (6) Hong, J.; Jin, C.; Yuan, J.; Zhang, Z., Atomic Defects in Two-Dimensional Materials: From Single-Atom Spectroscopy to Functionalities in Opto-/Electronics, Nanomagnetism, and Catalysis. *Adv. Mater.* **2017**, *29*, 1606434.
- (7) Cowley, R. A.; Buyers, W. J. L., The Properties of Defects in Magnetic Insulators. *Rev. Mod. Phys.* **1972**, *44*, 406-450.
- (8) Wiesendanger, R., Nanoscale Magnetic Skyrmions in Metallic Films and Multilayers: A New Twist for Spintronics. *Nat. Rev. Mater.* **2016**, *1*, 16044.
- (9) Lima Fernandes, I.; Bouaziz, J.; Blügel, S.; Lounis, S., Universality of Defect-Skyrmion Interaction Profiles. *Nat. Commun.* **2018**, *9*, 4395.
- (10) Song, T.; Cai, X.; Tu, M. W.-Y.; Zhang, X.; Huang, B.; Wilson, N. P.; Seyler, K. L.; Zhu, L.; Taniguchi, T.; Watanabe, K.; McGuire, M. A.; Cobden, D. H.; Xiao, D.; Yao, W.; Xu, X., Giant Tunneling Magnetoresistance in Spin-Filter van der Waals Heterostructures. *Science* **2018**, *360*, 1214-1218.
- (11) Huang, B.; McGuire, M. A.; May, A. F.; Xiao, D.; Jarillo-Herrero, P.; Xu, X., Emergent Phenomena and Proximity Effects in Two-Dimensional Magnets and Heterostructures. *Nat. Mater.* **2020**, *19*, 1276-1289.
- (12) Gibertini, M.; Koperski, M.; Morpurgo, A. F.; Novoselov, K. S., Magnetic 2D materials and heterostructures. *Nat. Nanotech.* **2019**, *14*, 408-419.
- (13) Gong, C.; Zhang, X., Two-dimensional magnetic crystals and emergent heterostructure devices. *Science* **2019**, *363*, eaav4450.
- (14) Wang, Q. H.; Bedoya-Pinto, A.; Blei, M.; Dismukes, A. H.; Hamo, A.; Jenkins, S.; Koperski, M.; Liu, Y.; Sun, Q.-C.; Telford, E. J.; Kim, H. H.; Augustin, M.; Vool, U.; Yin, J.-X.; Li, L. H.; Falin, A.; Dean, C. R.; Casanova, F.; Evans, R. F. L.; Chshiev, M.; Mishchenko, A.; Petrovic, C.; He, R.; Zhao, L.; Tsen, A. W.; Gerardot, B. D.; Brotons-Gisbert, M.; Guguchia, Z.; Roy, X.; Tongay, S.; Wang, Z.; Hasan, M. Z.; Wrachtrup, J.; Yacoby, A.; Fert, A.; Parkin, S.; Novoselov, K. S.; Dai, P.; Balicas, L.; Santos, E. J. G., The Magnetic Genome of Two-Dimensional van der Waals Materials. *ACS Nano* **2022**, *16*, 6960-7079.

- (15) Huang, B.; Clark, G.; Navarro-Moratalla, E.; Klein, D. R.; Cheng, R.; Seyler, K. L.; Zhong, D.; Schmidgall, E.; McGuire, M. A.; Cobden, D. H.; Yao, W.; Xiao, D.; Jarillo-Herrero, P.; Xu, X., Layer-Dependent Ferromagnetism in a van der Waals Crystal Down to the Monolayer Limit. *Nature* **2017**, *546*, 270-273.
- (16) Sivadas, N.; Okamoto, S.; Xu, X.; Fennie, C. J.; Xiao, D., Stacking-Dependent Magnetism in Bilayer CrI₃. *Nano Lett.* **2018**, *18*, 7658-7664.
- (17) Seyler, K. L.; Zhong, D.; Huang, B.; Linpeng, X.; Wilson, N. P.; Taniguchi, T.; Watanabe, K.; Yao, W.; Xiao, D.; McGuire, M. A.; Fu, K.-M. C.; Xu, X., Valley Manipulation by Optically Tuning the Magnetic Proximity Effect in WSe₂/CrI₃ Heterostructures. *Nano Lett.* **2018**, *18*, 3823-3828.
- (18) McGuire, M. A.; Dixit, H.; Cooper, V. R.; Sales, B. C., Coupling of Crystal Structure and Magnetism in the Layered, Ferromagnetic Insulator CrI₃. *Chem. Mater.* **2015**, *27*, 612-620.
- (19) Dillon, J. F.; Kamimura, H.; Remeika, J. P., Magneto-Optical Properties of Ferromagnetic Chromium Trihalides. *J. Phys. Chem. Solids* **1966**, *27*, 1531-1549.
- (20) Suits, J., Faraday and Kerr Effects in Magnetic Compounds. *IEEE Trans. Mag.* **1972**, *8*, 95-105.
- (21) Güdel, H. U.; Snellgrove, T. R., Jahn-Teller Effect in the ⁴T_{2g} State of Chromium(III) in Dicesium Sodium Indium(III) Hexachloride. *Inorg. Chem.* **1978**, *17*, 1617-1620.
- (22) Peng, B.; Chen, Z.; Li, Y.; Liu, Z.; Liang, D.; Deng, L., Multiwavelength Magnetic Coding of Helical Luminescence in Ferromagnetic 2D Layered CrI₃. *iScience* **2022**, *25*, 103623.
- (23) Wyart, J.-F.; Tchang-Brillet, W.-Ü. L.; Spector, N.; Palmeri, P.; Quinet, P.; Biémont, E., Extended Analysis of the Spectrum of Triply-ionized Ytterbium (Yb IV) and Transition Probabilities. *Phys. Scripta* **2001**, *63*, 113-121.
- (24) Georgescu, A. B.; Millis, A. J.; Rondinelli, J. M., Trigonal Symmetry Breaking and Its Electronic Effects in the Two-Dimensional Dihalides MX₂ and Trihalides MX₃. *Phys. Rev. B* **2022**, *105*, 245153.
- (25) Bronova, A.; Bredow, T.; Glaum, R.; Riley, M. J.; Urland, W., BonnMag: Computer Program for Ligand-Field Analysis of fⁿ Systems Within the Angular Overlap Model. *J. Comp. Chem.* **2018**, *39*, 176-186.
- (26) Zhang, Y.; Wu, X.; Lyu, B.; Wu, M.; Zhao, S.; Chen, J.; Jia, M.; Zhang, C.; Wang, L.; Wang, X.; Chen, Y.; Mei, J.; Taniguchi, T.; Watanabe, K.; Yan, H.; Liu, Q.; Huang, L.; Zhao, Y.; Huang, M., Magnetic Order-Induced Polarization Anomaly of Raman Scattering in 2D Magnet CrI₃. *Nano Lett.* **2020**, *20*, 729-734.
- (27) Al-Mobarak, R.; Warren, K. D., The Effect of Covalency on the Spin—Orbit Coupling Constant. *Chem. Phys. Lett.* **1973**, *21*, 513-516.
- (28) Bungenstock, C.; Tröster, T.; Holzapfel, W. B., Effect of Pressure on Free-Ion and Crystal-Field Parameters of Pr³⁺ in LOCl (L = La, Pr, Gd). *Phys. Rev. B* **2000**, *62*, 7945-7955.
- (29) Schwartz, R. W., Electronic Structure of the Octahedral Hexachloroytterbate Ion. *Inorg. Chem.* **1977**, *16*, 1694-1698.
- (30) Kanellakopoulos, B.; Amberger, H. D.; Rosenbauer, G. G.; Fischer, R. D., Zur Elektronenstruktur hochsymmetrischer Verbindungen der Lanthanoiden und Actinoiden—V: Paramagnetische Suszeptibilität und elektronisches Raman-Spektrum von Cs₂NaYb(III)Cl₆. *J. Inorg. Nuc. Chem.* **1977**, *39*, 607-611.
- (31) Tsujii, N.; Imanaka, Y.; Takamasu, T.; Kitazawa, H.; Kido, G., Photoluminescence of Yb³⁺-Doped CuInS₂ Crystals in Magnetic Fields. *J. Appl. Phys.* **2001**, *89*, 2706-2710.

- (32) Haumesser, P.-H.; Gaumé, R.; Viana, B.; Antic-Fidancev, E.; Vivien, D., Spectroscopic and Crystal-Field Analysis of New Yb-doped Laser Materials. *J. Phys.: Cond. Mat.* **2001**, *13*, 5427-5447.
- (33) de Maat-Gersdorf, I. Spectroscopic Analysis of Erbium-Doped Silicon and Ytterbium Doped Indium Phosphide. University of Amsterdam, 2001.
- (34) Liu, Y.; Petrovic, C., Three-Dimensional Magnetic Critical Behavior in CrI₃. *Phys. Rev. B* **2018**, *97*, 014420.
- (35) Coey, J. M. D., *Magnetism and Magnetic Materials*. Cambridge University Press 2010.
- (36) Lado, J. L.; Fernández-Rossier, J., On the Origin of Magnetic Anisotropy in Two Dimensional CrI₃. *2D Mater.* **2017**, *4*, 035002.
- (37) Aebersold, M. A.; Güdel, H. U.; Hauser, A.; Furrer, A.; Blank, H.; Kahn, R., Exchange Interactions in Mixed Yb³⁺-Cr³⁺ and Yb³⁺-Ho³⁺ Dimers: An Inelastic-Neutron-Scattering Investigation of Cs₃Yb_{1.8}Cr_{0.2}Br₉ and Cs₃Yb_{1.8}Ho_{0.2}Br₉. *Phys. Rev. B* **1993**, *48*, 12723-12731.
- (38) Mironov, V. S.; Chibotaru, L. F.; Ceulemans, A., Exchange Interaction in the YbCrBr₉³⁻ Mixed Dimer: The Origin of a Strong Yb³⁺-Cr³⁺ Exchange Anisotropy. *Phys. Rev. B* **2003**, *67*, 014424.
- (39) Atanasov, M.; Daul, C.; Güdel, H. U., Modelling of Anisotropic Exchange Coupling in Rare-Earth -Transition-Metal Pairs: Applications to Yb³⁺-Mn²⁺ and Yb³⁺-Cr³⁺ Halide Clusters and Implications to the Light Up-Conversion. In *Comp. Chem.: Rev. Current Trends*, World Scientific: 2005; Vol. 9, pp 153-194.
- (40) Cao, S.; Sinha, K.; Zhang, X.; Zhang, X.; Wang, X.; Yin, Y.; N'Diaye, A. T.; Wang, J.; Keavney, D. J.; Paudel, T. R.; Liu, Y.; Cheng, X.; Tsymbal, E. Y.; Dowben, P. A.; Xu, X., Electronic Structure and Direct Observation of Ferrimagnetism in Multiferroic Hexagonal YbFeO₃. *Phys. Rev. B* **2017**, *95*, 224428.
- (41) Dalal, B.; Sarkar, B.; Dev Ashok, V.; De, S. K., Evolution of Magnetic Properties and Exchange Interactions in Ru Doped YbCrO₃. *J. Phys.: Cond. Mat.* **2016**, *28*, 426001.
- (42) Imbusch, G. F.; Yen, W. M.; Schawlow, A. L.; McCumber, D. E.; Sturge, M. D., Temperature Dependence of the Width and Position of the ²E → ⁴A₂ Fluorescence Lines of Cr³⁺ and V²⁺ in MgO. *Phys. Rev.* **1964**, *133*, A1029-A1034.
- (43) Böttger, T.; Thiel, C. W.; Cone, R. L.; Sun, Y.; Faraon, A., Optical Spectroscopy and Decoherence Studies of Yb³⁺:YAG at 968 nm. *Phys. Rev. B* **2016**, *94*, 045134.
- (44) Fisher, M. E., The Theory of Equilibrium Critical Phenomena. *Rep. Prog. Phys.* **1967**, *30*, 615-730.
- (45) Bermudez, V. M.; McClure, D. S., Spectroscopic studies of the two-dimensional magnetic insulators chromium trichloride and chromium tribromide—II. *J. Phys. Chem. Solids* **1979**, *40*, 149-173.

Table of Contents Graphic



Magnetic Amplification at Yb³⁺ "Designer Defects" in the van der Waals Ferromagnet, CrI₃

Kimo Pressler, Thom J. Snoeren, Kelly M. Walsh, Daniel R. Gamelin*
Department of Chemistry, University of Washington, Seattle, WA 98195, United States
Email: gamelin@uw.edu

Experimental Methods

General Considerations. All sample preparation and manipulation was performed in a glovebox under an atmosphere of purified dinitrogen.

Chemicals. Chromium metal powder (200 mesh, 99.94%, lot X15E028) was purchased from Alfa Aesar. According to the manufacturer's certificate of analysis, the majority of the impurity in this sample lot was Ni at 343 ppm. A chromium chip (99.995%, lot MKCH4484) was also purchased from Sigma Aldrich as a higher-purity Cr source. The Cr chip was ground to a powder using a mortar and pestle and used in an analogous manner as the powder precursor. I₂ (≥99.99%) was purchased from Sigma Aldrich. Ytterbium metal powder 40 mesh (99.9%) was purchased from BeanTown chemical. All chemicals were used as received without further purification.

Synthesis of CrI₃ and Yb³⁺-Doped CrI₃ Single Crystals. Single crystals of the doped and undoped CrI₃ were grown by chemical vapor transport in a manner similar to that described in previous literature reports.¹ For undoped CrI₃, Cr(0) metal and I₂ were loaded as a 1:3 stoichiometric ratio into a quartz tube and sealed under an evacuated atmosphere. For Yb³⁺-doped CrI₃, additional Yb(0) metal was loaded along with the other starting materials. The quartz tubes were 15 cm long with inner and outer diameters of 14 and 16 mm, respectively. Sealed tubes were placed in an open-ended horizontal tube furnace with the starting materials in the hot zone set at 650 °C and the other end at a temperature of ca. 500 °C. Samples were heated for 5 days and then allowed to slowly cool to room temperature. Once cooled, the tubes were brought into a glove box and cracked open to yield shiny dark plate-like crystals that had formed at the cold end of the quartz tube. Elemental analysis of the Yb³⁺-doped samples was performed by inductively coupled plasma mass spectrometry (ICP-MS) using a PerkinElmer NexION 2000B. Samples were prepared by digesting single crystals in concentrated nitric acid with sonication and then further diluted in ultrapure H₂O. Yb³⁺ doping levels are reported as cation mole fraction, [Yb³⁺]/([Cr³⁺]+[Yb³⁺]), in percentage, with an estimated uncertainty of ±0.1%. Crystal thickness was measured by mounting a representative flake to a glass slide using double-sided tape and imaging the flake with an optical microscope in a glovebox at various magnifications. The edge length was calculated in ImageJ² using known pixel resolutions.

X-ray Diffraction (XRD) Characterization. Samples were prepared for XRD on the powder diffractometer by placing single crystals onto silicon substrates and sealing under Kapton films to reduce exposure to air. Data were collected using a Bruker D8 Discover powder diffractometer with a high-efficiency I μ S microfocus x-ray source for Cu K α radiation (50 kV, 1 mA). For single-crystal XRD, a crystal measuring 0.10 x 0.05 x 0.01 mm³ was mounted on a loop with oil. Data were collected at 263 K on a Bruker APEX II single-crystal X-ray diffractometer using Mo-radiation, equipped with a Miracol X-ray optical collimator. The data were integrated and scaled using SAINT, SADABS within the APEX2 software package by

Bruker.³ Solution by direct methods (SHELXT^{4, 5} or SIR97^{6, 7}) produced a complete heavy-atom phasing model consistent with the proposed structure. The structure was completed by difference Fourier synthesis with SHELXL.^{8, 9} Scattering factors are from Waasmair and Kirfel.¹⁰ All atoms were refined anisotropically by full-matrix least-squares.

Including intrinsic disorder, a least squares refinement optimization of the data yields the lattice structure that we report. From the 983 reflections collected covering the indices, $-8 \leq h \leq 8$, $-14 \leq k \leq 14$, $-8 \leq l \leq 8$, 518 reflections were found that were symmetry independent and an R_1 value of 0.0521 was obtained, indicating a good fit. R_1 is calculated as:

$$R_1 = \frac{\sum ||F_{obs}| - |F_{calc}||}{\sum |F_{obs}|}$$

There is no detectable electron density between layers, indicating that Yb^{3+} does not intercalate between layers in CrI_3 .

Variable-Temperature Photoluminescence (VTPL). Samples for VTPL measurements were prepared by placing a single crystal between two quartz disks and loading into a closed-cycle helium cryostat. PL spectra were collected by exciting the sample with a continuous-wave 660 nm (1.88 eV) diode at 4 mW/cm². Emission was collected and focused into a monochromator with a spectral bandwidth of 0.627 nm and detected by a Hamamatsu InGaAs/InP NIR photomultiplier tube, with signal recorded using a photon counter. Temperature was varied from 4 to 300 K, starting at low temperature. All spectra were corrected for instrument response.

Magnetic Circularly Polarized Luminescence (MCPL). Samples for MCPL measurements were prepared as single crystals placed between two quartz disks and loaded into a superconducting magneto-optical cryostat (Cryo-Industries SMC-1659 OVT) oriented in the Faraday configuration. For full-spectrum measurements at static fields, samples were excited with a 660 nm (1.88 eV) diode at approximately 40 mW/cm². For field-sweep measurements, samples were excited with a linearly polarized HeNe laser (632.8 nm/1.96 eV, 27 mW/cm² for -6 to +6 T scans, 55 mW/cm² for -0.4 to +0.4 T scans). No distinguishable difference was found in either the PL spectra or variable-field data between the two excitation sources. For field-sweep measurements, the monochromator was centered at 1.117 eV with a 6 nm spectral bandwidth, and the signal was continuously monitored as the field was swept at a rate of 0.10 T/min and 0.45 T/min for the 0.4 T and 6 T scans, respectively. PL was collected along the magnetic-field axis and passed through a liquid-crystal variable retardation plate set at $\lambda/4$, followed by a linear polarizer to separate the left- and right-circularly polarized components. The PL was then focused into a fiber-optic cable and fed into a monochromator with a spectral bandwidth of 0.627 nm and detected by a Hamamatsu InGaAs/InP NIR photomultiplier, with signals recorded using a photon counter. Polarization ratios are defined as $\rho = (\sigma^- - \sigma^+)/(\sigma^- + \sigma^+) = (I_L - I_R)/(I_L + I_R) = \Delta I/I$, following the sign conventions outlined in Piepho and Schatz.¹¹

Magnetic Measurements. Magnetic data on individual single-crystal flakes (Fig. 1) were collected using a Quantum Design PPMS DynaCool vibrating sample magnetometer (VSM). A flake was affixed to the end of a quartz paddle with varnish (VGE 7031). The paddle was then snapped into the VSM brass sample holder with another quartz paddle placed symmetrically above the sample. The weak background signal from the sample holder was removed in the data analysis. The sample was probed with the external field aligned perpendicular to the face of the crystal, and magnetization data were collected as a function of applied field and temperature. The masses of individual flakes are below 0.1 mg and could not be accurately measured, so the magnetic data are reported in units of emu.

Ligand-field calculations within the Angular Overlap Model (AOM). Yb^{3+} ligand(crystal)-field energies and g factors were calculated using the BonnMag package.¹² Crystallographic data¹³ on CrI_3 were used to create an $[\text{YbI}_6]^{3-}$ unit with reduced symmetry (point group C_2). Crystallographic parameters were not adjusted for size differences between Cr^{3+} and Yb^{3+} . The electronic structure of Yb^{3+} was calculated using the spin-orbit coupling parameter ζ as well as AOM parameters e_σ and e_π to describe σ and π interactions with the Γ ligands, respectively. The value for e_π was taken to be isotropic. The Slater-Condon-Shortley (SCS) parameters F_2 , F_4 , and F_6 were taken to be 0, as is typically the case for Yb^{3+} ($4f^{13}$ configuration). The Stevens orbital reduction factor k was taken to be equal to 1.0. Increasing (decreasing) ζ while keeping all other parameters constant results in an increase (decrease) in all transition energies while retaining peak splitting energies. Adjusting e_σ or e_π alters the relative energies of the peaks but maintains the barycenters.

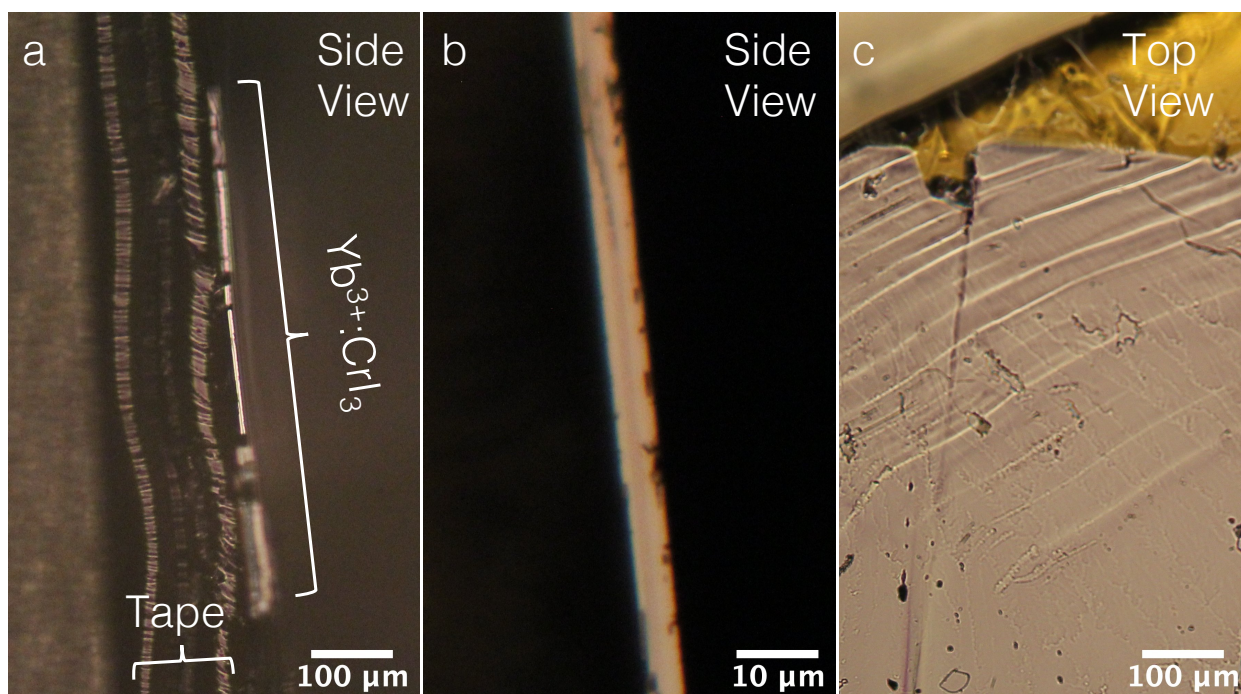


Figure S1. Images of an individual $\text{Yb}^{3+}:\text{CrI}_3$ single-crystal flake under an optical microscope at various magnification levels, viewing the flake's (a,b) edge, and (c) face. The flake thickness is estimated to be $5.1 \pm 0.3 \mu\text{m}$.

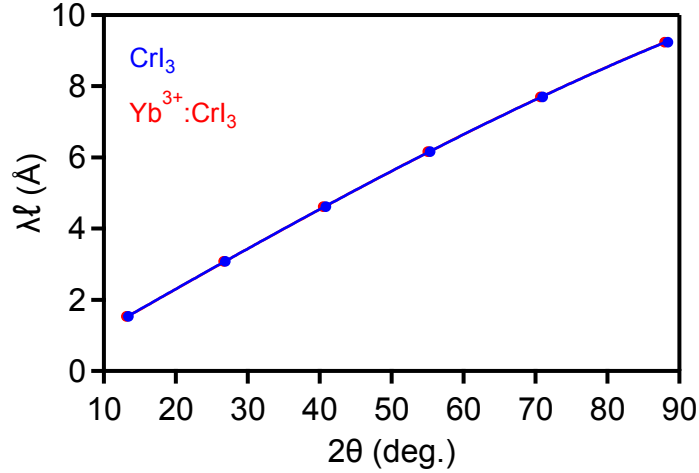


Figure S2. Analysis of XRD reflections collected using a powder diffractometer for 4.9% Yb³⁺-doped and undoped CrI₃ single-crystal flakes (same data as shown in Fig. 1bc). Using the method described by Jesche,¹⁴ the lattice parameter c for oriented single crystals with a monoclinic space group can be extracted from XRD data from a powder diffractometer using the following equation:

$$2c \cdot \sin\beta \cdot \sin\left(\theta - S \frac{\cos\theta}{2}\right) = \lambda\ell$$

Here, β is the obtuse angle in the monoclinic unit cell (108.507° for CrI₃), λ is the x-ray wavelength (Cu, 1.5406 \AA), ℓ is the Miller index of each reflection in the XRD spectrum and $S \frac{\cos\theta}{2}$ is a correction factor related to the displacement of the x-ray focal plane relative to the sample surface. Plotting 2θ values of the peak maxima vs $\lambda\ell$, the data can be fit using the equation above. For fitting, β and θ were taken in radians. By this method, the c lattice parameters were found to be 6.996 ± 0.002 and $7.013 \pm 0.002 \text{ \AA}$ for the undoped and doped samples, respectively. From the lattice parameter c , the position of the (00ℓ) powder diffractometer XRD peaks for a monoclinic single crystal can be calculated using the following equation:

$$2\theta = 2\sin^{-1}\left(\frac{\lambda}{2\sin\beta c} \ell\right)$$

The zero-shift in 2θ was determined by adding an offset to the experimental 2θ values and adjusting the offset to minimize the difference between experimental and calculated peak positions across all peaks in the XRD spectrum. This offset accounts for the measurement discrepancy due to the thickness of the single crystals displacing the x-ray focal plane. For CrI₃, a zero-shift of -0.015° was found, contrasted to a zero-shift of $+0.164^\circ$ for Yb³⁺-doped CrI₃. The displacement-corrected XRD spectra are shown in Fig. 1c in the main text.

Table S1. Single-crystal X-ray diffraction data for 2.5% $\text{Yb}^{3+}:\text{CrI}_3$ measured at 263 K, compared to literature data for CrI_3 .

	$\text{Yb}^{3+}:\text{CrI}_3$	CrI_3 (250 K, ref. ¹³)
Space group	$C2/m$	$C2/m$
a	6.86 Å	6.87 Å
b	11.89 Å	11.89 Å
c	6.99 Å	6.98 Å
α	90.0°	90.0°
β	108.7°	108.5°
γ	90.0°	90.0°
$[(\text{Yb}/\text{Cr}) - \text{Cr}]_{\text{avg}}$	3.96 Å	3.96 Å
$[(\text{Yb}/\text{Cr}) - \text{I}]_{\text{avg}}$	2.72 Å	2.72 Å
$[(\text{Yb}/\text{Cr}) - \text{I} - (\text{Yb}/\text{Cr})]_{\text{avg}}$	93.3°	93.6°
$[\text{I} - (\text{Yb}/\text{Cr}) - \text{I}]_{\text{avg}}$	86.8°	86.9°

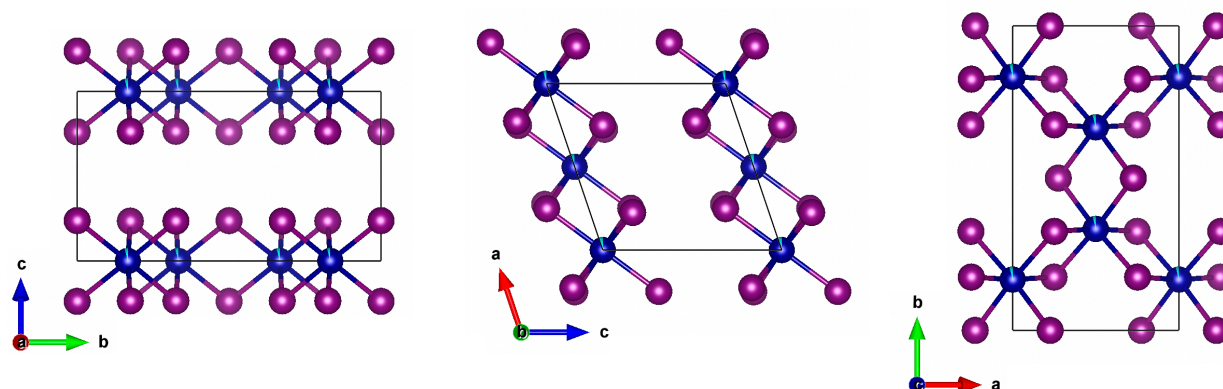


Figure S3. Visualization of the experimental room-temperature single-crystal XRD structure as viewed along the a , b , and c principal axes (left to right). Yb^{3+} (cyan) is found to substitute for Cr^{3+} (blue) in the edge-sharing octahedra formed by I^- (purple) anions. No excess electron density is observed between layers. Intralayer disorder is observed. The structure refines to the expected high-temperature $C2/m$ monoclinic symmetry. Some intralayer disorder was observed (not shown).

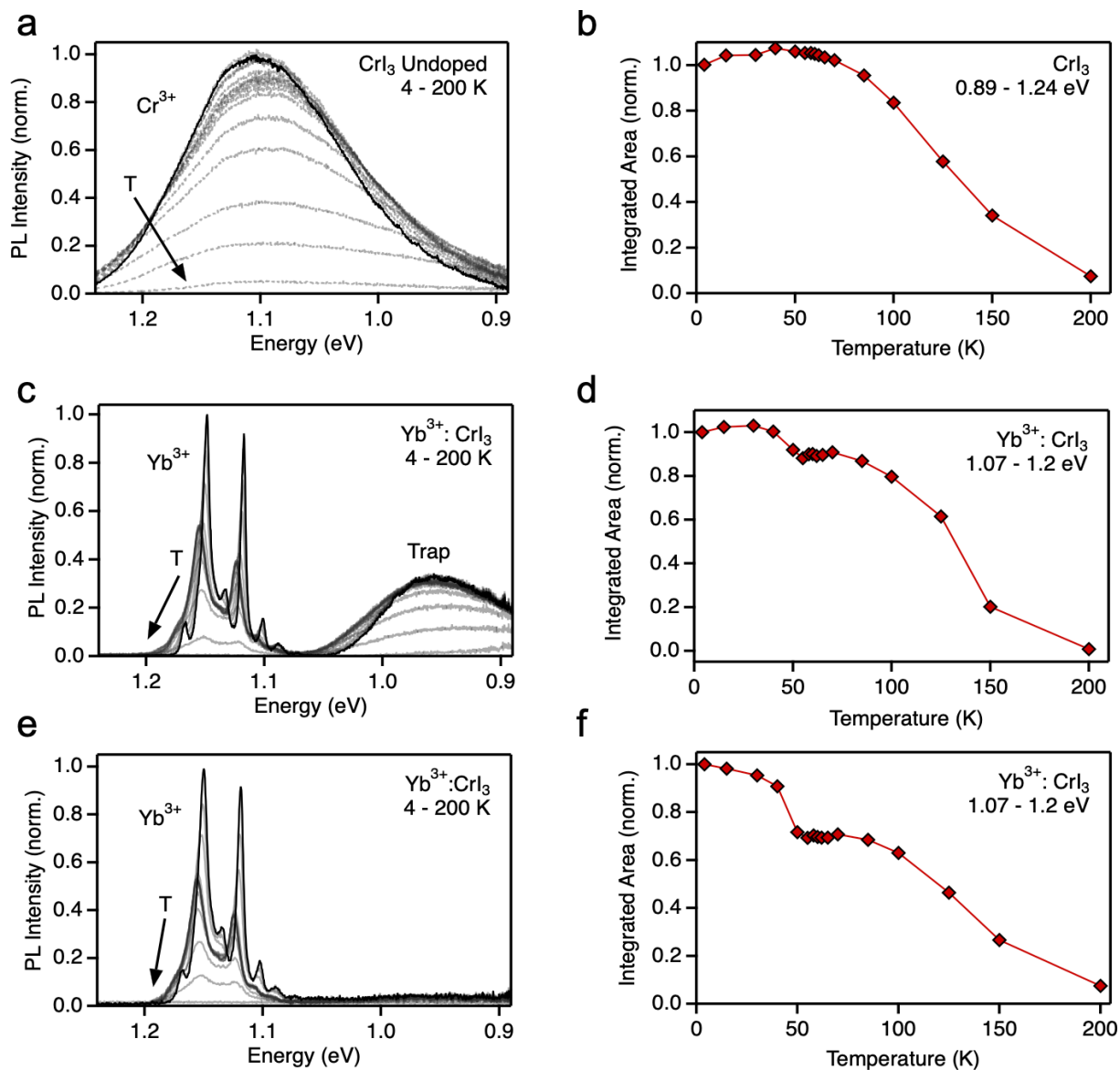


Figure S4. (a) Variable-temperature PL spectra of CrI_3 measured from 4 to 200 K under 1.88 eV CW excitation (from Fig. 2 of the main text). (b) Scatter plot depicting total integrated area of the CrI_3 PL from panel (a). The 200 K intensity is 7.5% that of the 4 K value. (c) Variable-temperature PL spectra of 4.9% $\text{Yb}^{3+}:\text{CrI}_3$ measured from 4 to 200 K under 1.88 eV CW excitation (from Fig. 2 of the main text). (d) Scatter plot depicting total integrated area of the Yb^{3+} PL from panel (c). The 200 K intensity is 0.8% that of the 4 K value. (e) Variable-temperature PL spectra of 5.0% $\text{Yb}^{3+}:\text{CrI}_3$ measured from 4 to 200 K under 1.88 eV CW excitation (from Fig. 2 of the main text). (f) Scatter plot depicting total integrated area of the Yb^{3+} PL from panel (e). The 200 K intensity is 7.5% that of the 4 K value. Note that a second, broad "trap" PL band is observed at ~ 0.98 eV in samples made from Cr metal powder precursor (99.94%, panel (c)) but not in samples made from Cr chip precursor (99.995%, panel (e)). Ni is the primary impurity in the powder precursor (see Methods), and Ni is detected in this CrI_3 sample at 0.4% cation mole fraction. $\text{Ni}^{2+} \ ^3\text{A}_{2g} \rightarrow \ ^3\text{T}_{2g}$ absorption in NiI_2 and $\text{Ni}^{2+}:\text{CdI}_2$ is centered around 0.93 eV,¹⁵ and the broad "trap" PL band in panel (c) is thus tentatively attributed to Ni^{2+} impurities in CrI_3 .

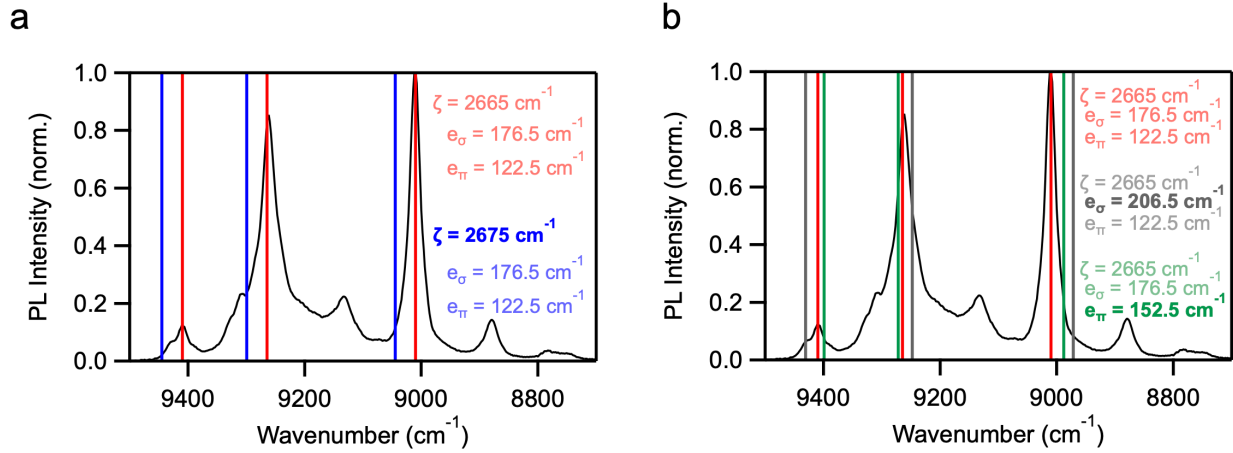


Figure S5. Comparison of the 5 K experimental data and calculated (AOM) f - f PL transition energies for 4.9% Yb³⁺:CrI₃. A best fit to the experimental PL data resulted in the following values: $\zeta = 2665 \text{ cm}^{-1}$ (330.4 meV), $e_{\sigma} = 176.5 \text{ cm}^{-1}$ (21.9 meV), $e_{\pi} = 122.5 \text{ cm}^{-1}$ (15.2 meV). The calculated transition energies using these parameters are shown as the vertical red lines in both panels. **(a)** Comparison of calculated transition energies obtained by changing from $\zeta = 2665 \text{ cm}^{-1}$ (red) to $\zeta = 2675 \text{ cm}^{-1}$ (blue), with all other parameters constant to the best-fit (red). **(b)** Comparison of calculated transition energies obtained by individually changing the values of e_{σ} and e_{π} . The gray traces show the effect of changing from $e_{\sigma} = 176.5 \text{ cm}^{-1}$ (red) to $e_{\sigma} = 206.5 \text{ cm}^{-1}$ with all other parameters constant to the best fit (red). The green traces show the effect of changing from $e_{\pi} = 122.5 \text{ cm}^{-1}$ (red) to $e_{\pi} = 152.5 \text{ cm}^{-1}$ with all other parameters constant to the best fit (red). From the best-fit parameters, g is anisotropic ($g_1 = 2.672$, $g_2 = 2.686$, $g_3 = 2.642$) and an average ground-state g value of ~ 2.7 is predicted.

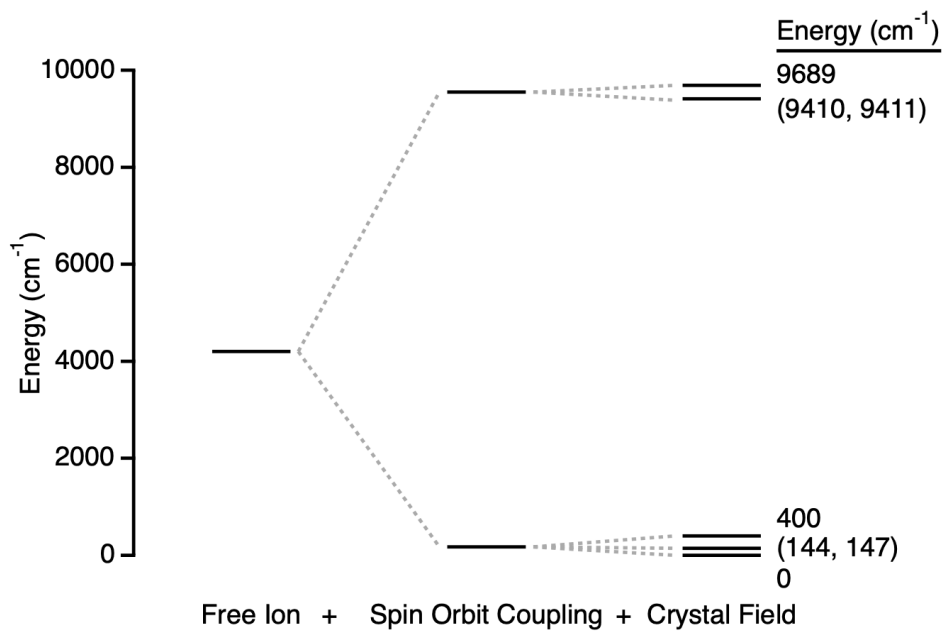


Figure S6. The Yb³⁺ valence energy level diagram described by the best-fit parameters of Fig. S5. The energies of the crystal field states in eV are: 0.0000, (0.0179, 0.0182), 0.0496, (1.1667, 1.1668), 1.2013 eV.

Table S2. Energies (cm⁻¹) of the valence electronic states, ²F_{5/2} and ²F_{7/2} barycenter energies,^a and ΔE(Barycenter) for Yb³⁺ ions in several host crystals, and for the free ion. These data were used to generate Fig. S7 (after converting to eV). Many of these entries are compiled in ref. 16.

Host Lattice	0	1	2	3	² F _{7/2} Barycenter	0'	1'	2'	² F _{5/2} Barycenter	ΔE(Bary)	ref.
Ca ₂ Ga ₂ SiO ₇ (CGS)	0.0	300	490	970	440	10250	10570	11010	10610	10170	17
SrLaGa ₃ O ₇ (SLG)	0.0	220	386	910	379	10190	10450	11025	10555	10176	17
Ca ₄ GdO(BO ₃) ₃ (GdCOB) (site I, Gd)	0.0	423	668	1003	524	10246	10706	11089	10680	10157	18
GdCOB (site II, Ca)	0.0	437	694	1003	534	10261	10737	11150	10716	10183	18
GdCOB (site III, Ca)	0.0	417	688	1003	527	10240	10682	11026	10649	10122	18
Ca ₄ YO(BO ₃) ₃ (YCOB)	0.0	427	556	1023	502	10242	10537	11109	10629	10128	19
Sc ₂ O ₃	0.0	474	634	1076	546	10250	10640	11198	10696	10150	20
Ca ₅ (PO ₄) ₃ F (CFAP)	0.0	409	597	1099	526	10178	10496	11069	10581	10055	21
Sr ₃ (PO ₄) ₃ F (SFAP)	0.0	362	618	1190	543	10150	10512	11108	10590	10048	22
Sr ₃ (VO ₄) ₃ F (SVAP)	0.0	321	562	1078	490	10141	10740	11050	10644	10153	23
Y ₃ Al ₅ O ₁₂ (YAG)	0.0	584	635	783	501	10328	10752	10917	10666	10165	24
BaCaBO ₃ F (BCBF)	0.0	303	533	902	435	10204	10570	11000	10591	10157	25
LiNbO ₃	0.0	352	448	788	397	10204	10471	11090	10588	10191	26
KGd(WO ₄) ₂ (KGW)	0.0	163	385	535	271	10188	10471	10682	10447	10176	27
KY(WO ₄) ₂ (KYW)	0.0	169	407	568	286	10187	10476	10695	10453	10167	27
CaWO ₄	0.0	220	366	492	270	10278	10366	10665	10436	10167	28
YAlO ₃	0.0	209	341	590	285	10220	10410	10730	10453	10168	28
LiYF ₄	0.0	216	371	479	267	10288	10409	10547	10415	10148	28
YAl ₃ (BO ₃) ₄ (YAB)	0.0	94	185	581	215	10194	10277	10672	10381	10166	29
Cs ₂ NaYbCl ₆	0	225	225	573	256	10243	10243	10708	10398	10142	30, 31
Cs ₃ Yb ₂ Br ₉	0.0	144	201	421	192	10277	10301	10578	10385	10194	32
CsCdBr ₃	0.0	114	140	441	174	10119	10146	10590	10285	10111	32
CuInS ₂	0.0	32	87	182	75	10033	10060	---	10095 ^a	10020	33
InP	0	35.5	35.5	97.5	42	10018	10064	10064	10049	10007	34
Free ion	---	---	---	---	0.0	---	---	---	10213	10213	35
CrI ₃	0.0	146	146	400	173	9410	---	---	9551 ^a	9379	this work

^aFor the entire data set of complete entries, the ratio of ²F_{5/2}:²F_{7/2} CF splitting energies, $(E(^2F_{5/2} \text{ Barycenter}) - E_0)/(E(^2F_{7/2} \text{ Barycenter}))$ is 0.82 ± 0.14 . The ²F_{5/2} barycenter energies for Yb³⁺:CrI₃ and Yb³⁺:CuInS₂ were thus set equal to the ²F_{7/2} barycenter energies for the same compounds. The resulting uncertainties in ΔE(Bary) are estimated to be < ~1%, close to or smaller than the data points in Fig. S7. For comparison, the Yb³⁺:CrI₃ AOM calculations above yield: ²F_{7/2} barycenter = 173 cm⁻¹ (21 meV), ²F_{5/2} barycenter = 9503 cm⁻¹ (1.178 eV), ΔE(Bary) = 9330 cm⁻¹ (1.157 eV), within this uncertainty range.

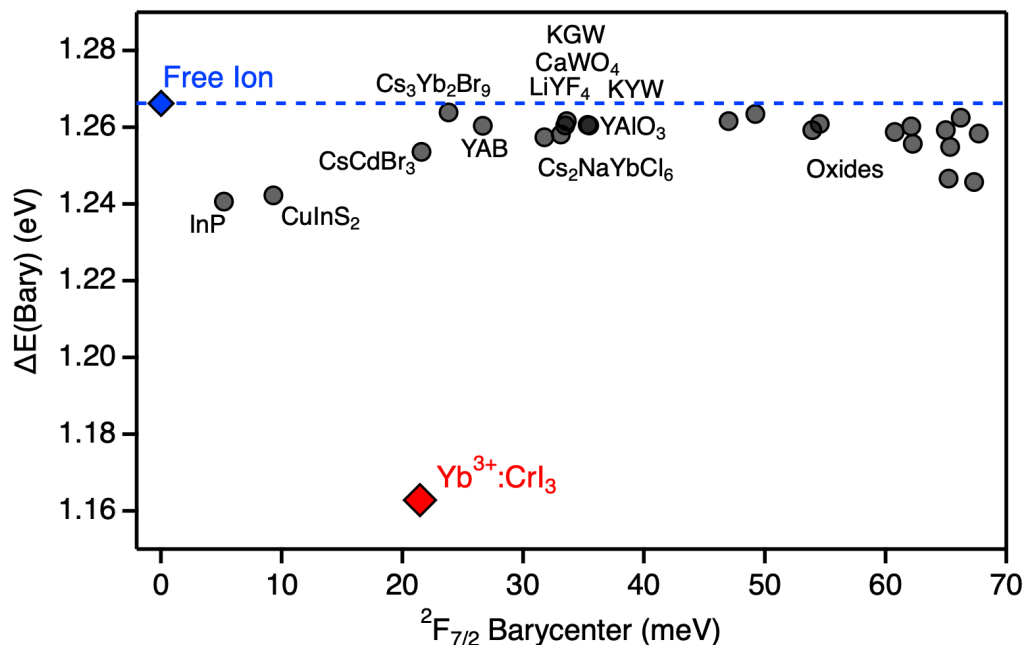


Figure S7. Plot of the difference between experimental $\text{Yb}^{3+} \ ^2F_{5/2}$ and $\ ^2F_{7/2}$ barycenter energies ($\Delta E(\text{Bary})$) for the compounds listed in Table S2, and for the free ion, vs the barycenter energy for the $\ ^2F_{7/2}$ ground multiplet. The compounds associated with select data points are labeled. The dashed blue line shows the value of the free ion.

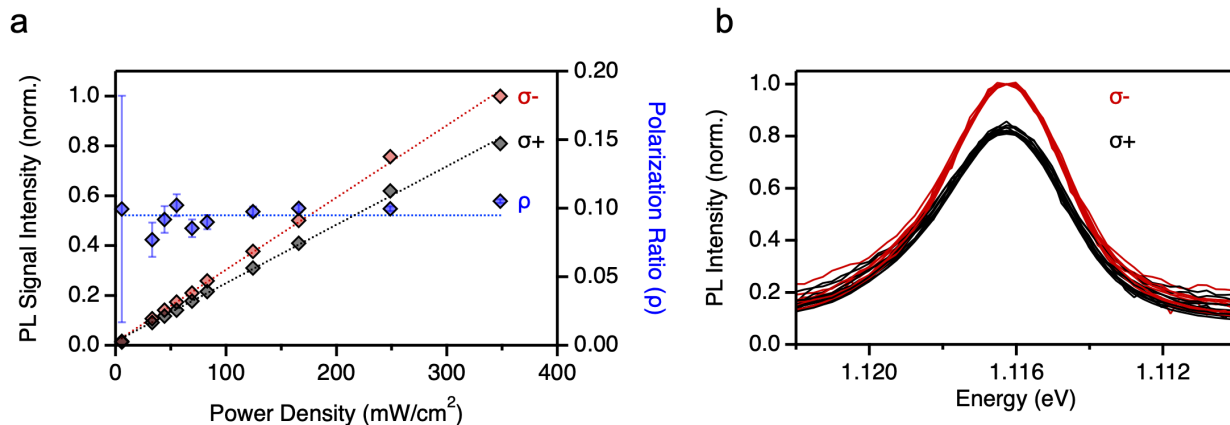


Figure S8. (a) Power dependence of σ^- (red) and σ^+ (black) PL peak intensities and circular polarization (ρ , blue) of the $\Gamma_8 \rightarrow \Gamma_7$ transition. The data were collected at 0.5 T and 5 K and the sample was excited with linearly polarized light at 1.96 eV. The PL intensities show a linear increase with power, resulting in a constant polarization ratio. The error bars represent uncertainty estimated from the linear fit of the polarization intensities. (b) The σ^- (red) and σ^+ (black) component of the $\Gamma_8 \rightarrow \Gamma_7$ transition normalized across all powers. The traces overlay each other well, showing no detectable power dependence.

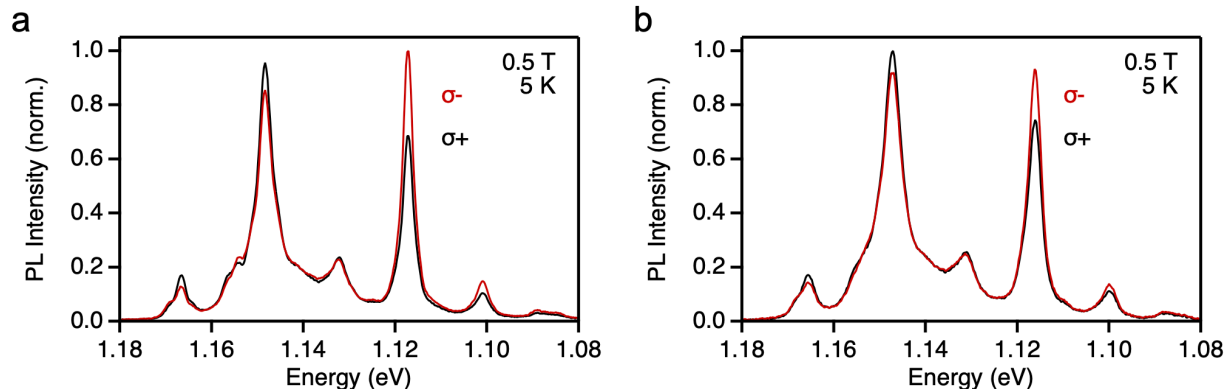


Figure S9. Comparison of full MCPL spectra across two different samples, measured at 0.5 T, 5 K. **(a)** The sample used in Fig. 3b,c,e,f of the main text. **(b)** The sample used in Fig. 3d of the main text. The two samples show very similar spectra, with slight differences in polarization magnitude.

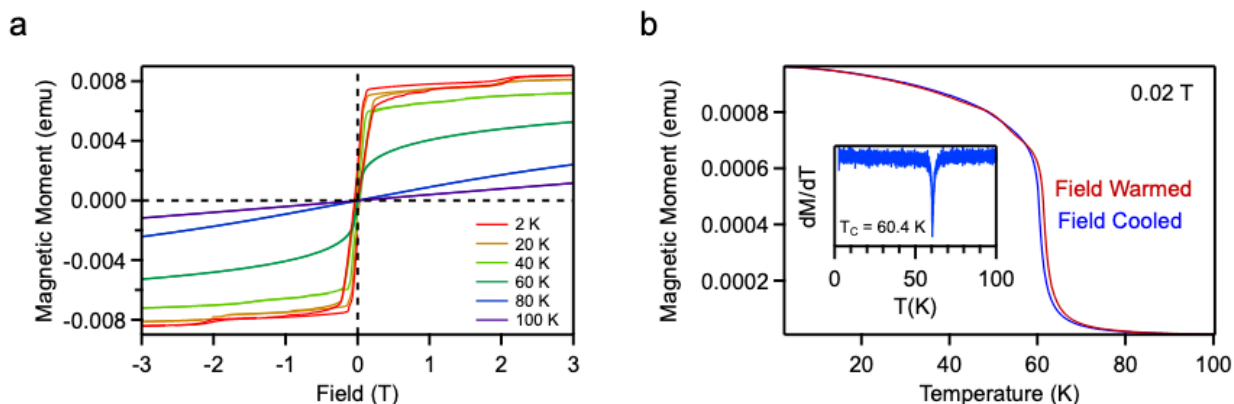


Figure S10. Magnetic data for a single-crystal flake of 5% $\text{Yb}^{3+}:\text{CrI}_3$, measured by VSM. The sample was probed with the external field aligned perpendicular to the face of the crystal. **(a)** Plots of magnetization vs external field measured at various temperatures. The data are similar to those collected on undoped CrI_3 bulk crystals (e.g., Fig S11). At 2 K, a coercive field of ~ 44 mT was found. **(b)** Plot of magnetization vs temperature measured in the field-cooled and field-warmed directions. The inset shows the derivative of the field-cooled data as a function of temperature, where the Curie temperature is found to be 60.4 K. These data show that Yb^{3+} doping has no significant effect on the magnetism of CrI_3 in these samples.

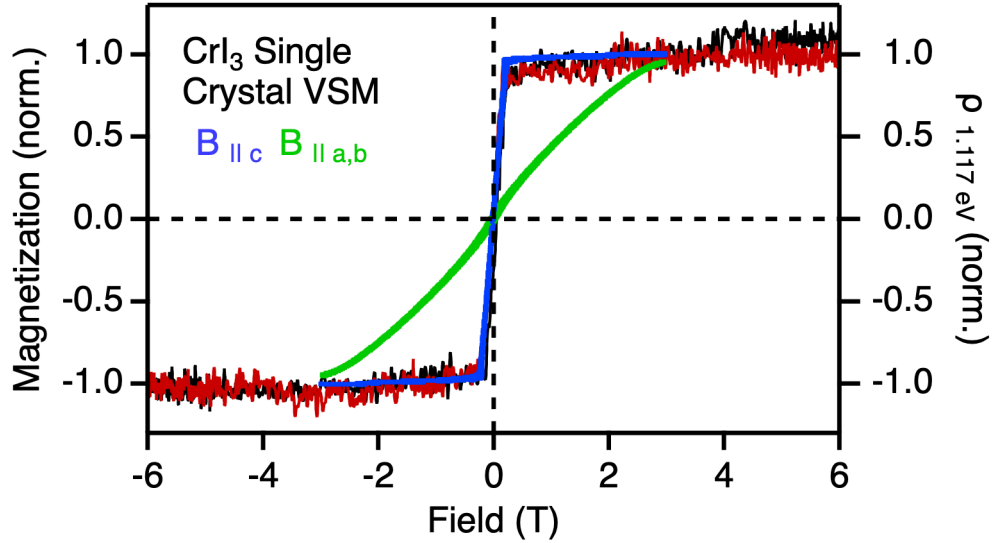


Figure S11. The same polarization data as featured in Fig. 3d of the main text, overlaid with CrI_3 magnetization data measured from -3 to +3 T with the field oriented parallel to the crystallographic c axis (blue) by single-crystal vibrating sample magnetometry (VSM).³⁶ For comparison, the magnetization perpendicular to c (green) is also shown. The Yb^{3+} MCPL polarization ρ is superimposable with the CrI_3 magnetization measured in the same configuration.

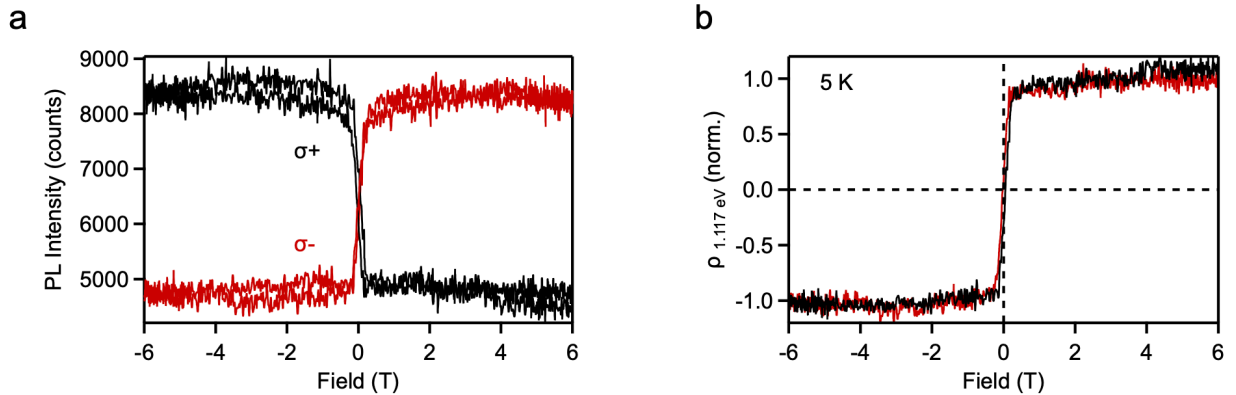


Figure S12. (a) Individual circularly polarized MCPL components measured during continuous field sweeps from -6 to +6 T and back at 5 K. (b) The same data, displayed as the polarization ratio (ρ , normalized). Panel (b) is shown as Fig. 3d of the main text. Data measured using 14 mW/cm^2 excitation.

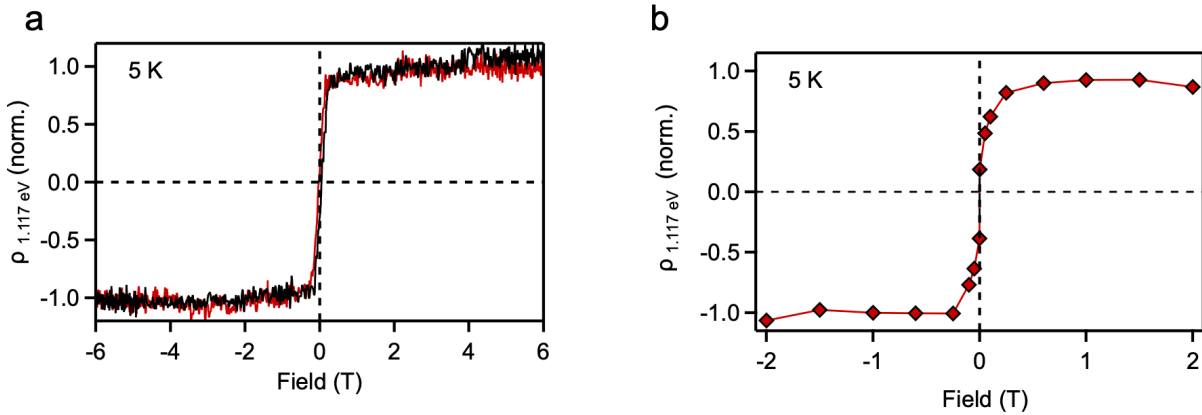


Figure S13. Comparison of field-dependent polarization ratios (ρ , normalized) measured with (a) linearly polarized and (b) unpolarized excitation at 5 K. In panel (b), no data were collected above 2 T. Panel (a) is shown as Fig. 3d of the main text.

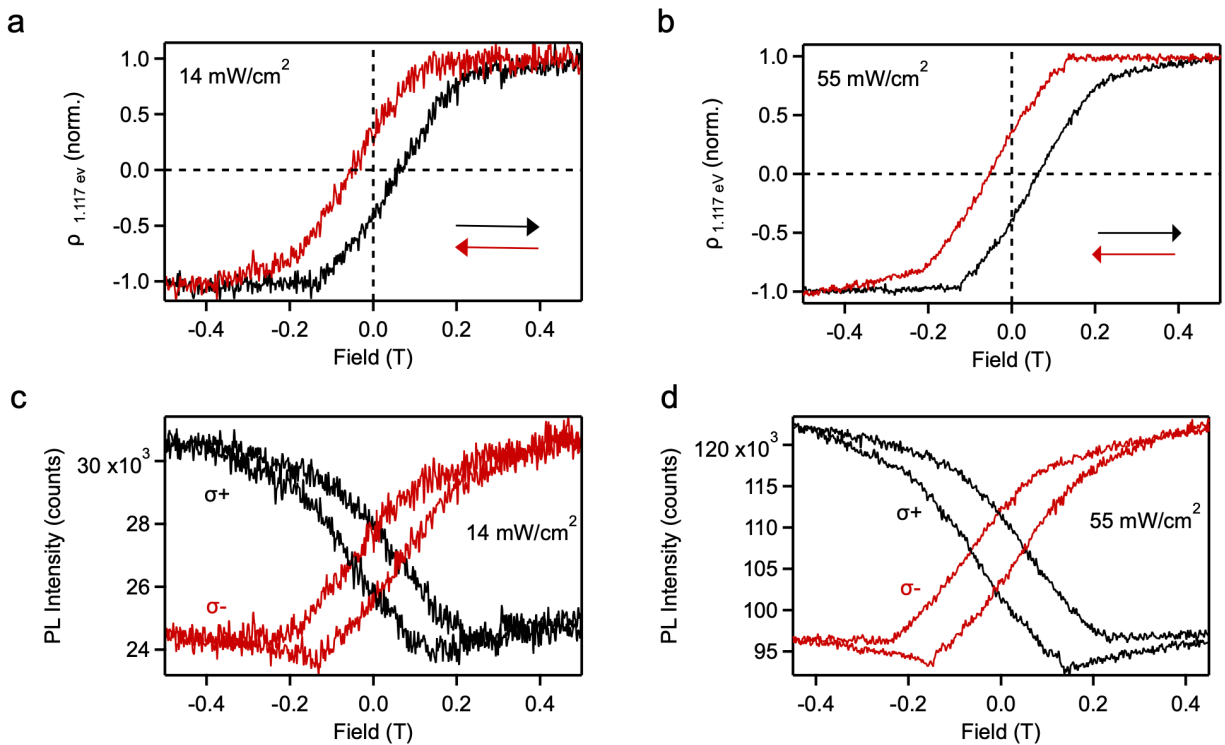


Figure S14. (a,b) Effect of excitation power on the polarization ratio (ρ , normalized). Magnetic hystereses measured under (a) low- and (b) higher-power excitation (14 vs 55 mW/cm², 5 K) show no difference. The black (red) trace corresponds to the sweep from negative (positive) to positive (negative) fields. (c, d) The separate circularly polarized PL components from the same (c) low- and (d) high-power measurements.

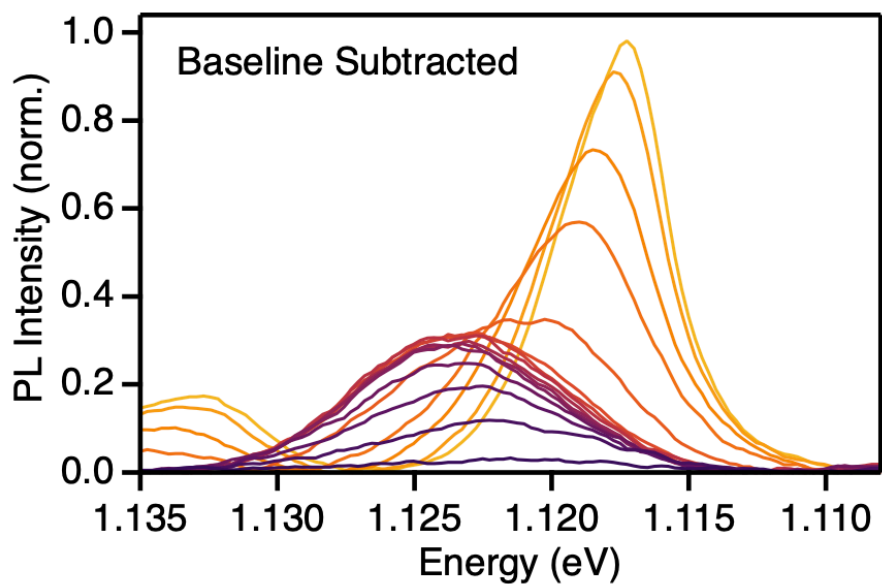


Figure S15. Temperature dependence of the $\Gamma_8 \rightarrow \Gamma_7$ PL feature of 4.9% $\text{Yb}^{3+}:\text{CrI}_3$ measured from 4 to 200 K under no external magnetic field (from Fig. 4 of the main text, $T = 4, 15, 30, 40, 50, 55, 58, 60, 62, 65, 70, 85, 100, 125, 150$ K). A linear baseline was subtracted from each spectrum here to facilitate viewing and determination of the peak's FWHM.

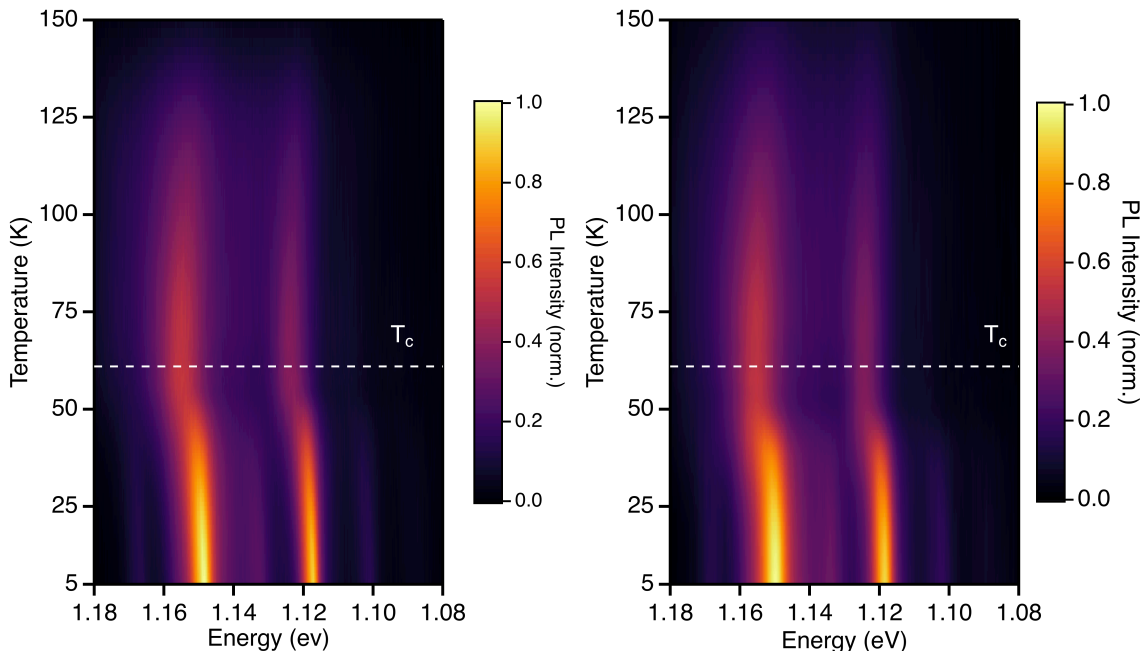


Figure S16. (a,b) False-color plots of the Yb^{3+} PL intensities vs temperature measured for the two samples shown in Fig. S4c,e, respectively, from 4 to 150 K at zero external magnetic field. The horizontal dashed line indicates $T_C = 61$ K. The two samples show the same temperature dependence, but the features are slightly better resolved in panel (a). Panel (a) is shown as Fig. 4a of the main text.

References

- (1) Seyler, K. L.; Zhong, D.; Klein, D. R.; Gao, S.; Zhang, X.; Huang, B.; Navarro-Moratalla, E.; Yang, L.; Cobden, D. H.; McGuire, M. A.; Yao, W.; Xiao, D.; Jarillo-Herrero, P.; Xu, X. Ligand-field helical luminescence in a 2D ferromagnetic insulator. *Nat. Physics* **2018**, *14* (3), 277-281.
- (2) Abramoff, M. D.; Magalhaes, P. J.; Ram, S. J. Image Processing with ImageJ. *Biophot. Int.* **2004**, *11* (7), 35-42.
- (3) Bruker. APEX2 (Version 2.1-4), SAINT (version 7.34A), SADABS (version 2007/4),. **2007**,
- (4) Sheldrick, G. M. A short history of SHELX. *Acta Cryst.* **2007**, *A64*, 112-122.
- (5) Sheldrick, G. M. SHELXT - Integrated space-group and crystal-structure determination. *Acta Cryst.* **2015**, *A71*, 3-8.
- (6) Altomare, A.; Cascarano, G. L.; Giacovazzo, C.; Guagliardi, A. Completion and refinement of crystal structures with SIR92. *J. Appl. Cryst.* **1993**, *26*, 343-350.
- (7) Altomare, A.; Burla, C.; Camalli, M.; Cascarano, G. L.; Giacovazzo, C.; Guagliardi, A.; Moliterni, A. G. G.; Polidori, G.; Spagna, R.; Burla, C.; Camalli, M.; Cascarano, G. L.; Giacovazzo, C.; Guagliardi, A.; Moliterni, A. G. G.; Polidori, G.; Spagna, R. SIR97: a new tool for crystal structure determination and refinement. *J. Appl. Crystallogr.* **1999**, (32), 115-119.
- (8) Sheldrick, G. M. SHELXL-97, Program for the Refinement of Crystal Structures. **1997**,
- (9) Sheldrick, G. M. Crystal structure refinement with SHELXL. *Acta Cryst.* **2015**, *C71*, 3-8.

- (10) Waasmaier, D.; Kirfel, A. New Analytical Scattering Factor Functions for Free Atoms and Ions. *Acta Crysta.* **1995**, *A51* (416-430),
- (11) Piepho, S. B.; Schatz, P. N. *Group theory in spectroscopy with applications to magnetic circular dichroism*; John Wiley & Sons, 1983.
- (12) Bronova, A.; Bredow, T.; Glaum, R.; Riley, M. J.; Urland, W. BonnMag: Computer program for ligand-field analysis of f^n systems within the angular overlap model. *J. Comp. Chem.* **2018**, *39* (3), 176-186.
- (13) McGuire, M. A.; Dixit, H.; Cooper, V. R.; Sales, B. C. Coupling of Crystal Structure and Magnetism in the Layered, Ferromagnetic Insulator CrI_3 . *Chem. Mater.* **2015**, *27* (2), 612-620.
- (14) Jesche, A. F., M.; Kreyssig, A.; Meier, W. R.; Canfield, P. C. X-Ray Diffraction on large single crystals using a powder diffractometer. *Philos. Mag. (Abingdon)* **2016**, *96* (20), 2115-2124.
- (15) Kuindersma, S. R.; Boudewijn, P. R.; Haas, C. Near-Infrared d-d Transitions of NiI_2 , $\text{CdI}_2:\text{Ni}^{2+}$, and CoI_2 . *Phys. stat. sol. (b)* **1981**, *108* (1), 187-194.
- (16) Haumesser, P.-H.; Gaumé, R.; Viana, B.; Antic-Fidancev, E.; Vivien, D. Spectroscopic and crystal-field analysis of new Yb-doped laser materials. *J. Phys.: Cond. Mat.* **2001**, *13* (23), 5427-5447.
- (17) Simondi-Teisseire, B. PhD Thesis. Paris VI University, 1996.
- (18) Mougél, F.; Dardenne, K.; Aka, G.; Kahn-Harari, A.; Vivien, D. Ytterbium-doped $\text{Ca}_4\text{GdO}(\text{BO}_3)_3$: an efficient infrared laser and self-frequency doubling crystal. *J. Opt. Soc. Am. B* **1999**, *16* (1), 164-172.
- (19) Mougél, F. PhD Thesis. Paris VI University, 1999
- (20) Mix, E. PhD Thesis. Hamburg University, 1999.
- (21) DeLoach, L. D.; Payne, S. A.; Chase, L. L.; Smith, L. K.; Kway, W. L.; Krupke, W. F. Evaluation of absorption and emission properties of Yb^{3+} doped crystals for laser applications. *IEEE J. Quant. Elect.* **1993**, *29* (4), 1179-1191.
- (22) Gruber, J. B.; Zandi, B.; Merkle, L. Crystal-field splitting of energy levels of rare-earth ions $\text{Dy}^{3+}(4f^9)$ and $\text{Yb}^{3+}(4f^{13})$ in M (II) sites in the fluorapatite crystal $\text{Sr}_5(\text{PO}_4)_3\text{F}$. *J. Appl. Phys.* **1998**, *83* (2), 1009-1017.
- (23) Payne, S. A.; DeLoach, L. D.; Smith, L. K.; Kway, W. L.; Tassano, J. B.; Krupke, W. F.; Chai, B. H. T.; Loutts, G. Ytterbium-doped apatite structure crystals: A new class of laser materials. *J. Appl. Phys.* **1994**, *76* (1), 497-503.
- (24) Bogomolova, G. A.; Bumagina, L. A.; Kaminskii, A. A.; Malkin, B. Z. Crystal field in laser garnets with TR^{3+} ions in the exchange charge model. *Sov. Phys. Solid State* **1977**, *19* (8), 1428-1435.
- (25) Schaffers, K. I.; DeLoach, L. D.; Payne, S. A. Crystal growth, frequency doubling, and infrared laser performance of $\text{Yb}^{3+}:\text{BaCaBO}_3\text{F}$. *IEEE J. Quant. Elect.* **1996**, *32* (5), 741-748.
- (26) Montoya, E.; Sanz-García, J.; Capmany, J.; Bausá, L.; Dening, A.; Kellner, T.; Huber, G. Continuous wave infrared laser action, self-frequency doubling, and tunability of $\text{Yb}^{3+}:\text{MgO}:\text{LiNbO}_3$. *J. Appl. Phys.* **2000**, *87* (9), 4056-4062.
- (27) Kuleshov, N. V.; Lagatsky, A. A.; Podlipensky, A. V.; Mikhailov, V. P.; Huber, G. Pulsed laser operation of Yb-doped $\text{KY}(\text{WO}_4)_2$ and $\text{KGd}(\text{WO}_4)_2$. *Optics lett.* **1997**, *22* (17), 1317-1319.

- (28) Morrison, C. A.; Leavitt, P. Handbook on the physics and chemistry of rare earths, ch 46. Amsterdam: Elsevier: 1982.
- (29) Wang, P.; Dawes, J. M.; Dekker, P.; Knowles, D. S.; Piper, J. A.; Lu, B. Growth and evaluation of ytterbium-doped yttrium aluminum borate as a potential self-doubling laser crystal. *J. Opt. Soc. Am. B* **1999**, *16* (1), 63-69.
- (30) Schwartz, R. W. Electronic structure of the octahedral hexachloroytterbate ion. *Inorg. Chem.* **1977**, *16* (7), 1694-1698.
- (31) Kanellakopulos, B.; Amberger, H. D.; Rosenbauer, G. G.; Fischer, R. D. Zur Elektronenstruktur hochsymmetrischer Verbindungen der Lanthanoiden und Actinoiden—V: Paramagnetische Suszeptibilität und elektronisches Raman-Spektrum von $\text{Cs}_2\text{NaYb(III)Cl}_6$. *J. Inorg. Nuc. Chem.* **1977**, *39* (4), 607-611.
- (32) Malkin, B. Z.; Leushin, A. M.; Iskhakova, A. I.; Heber, J.; Altwein, M.; Moller, K.; Fazlizhanov, I. I.; Ulanov, V. A. EPR and optical spectra of Yb^{3+} in CsCdBr_3 : Charge-transfer effects on the energy-level structure of Yb^{3+} in the symmetrical pair centers. *Phys. Rev. B* **2000**, *62* (11), 7063.
- (33) Tsujii, N.; Imanaka, Y.; Takamasu, T.; Kitazawa, H.; Kido, G. Photoluminescence of Yb^{3+} -doped CuInS_2 crystals in magnetic fields. *J. Appl. Phys.* **2001**, *89* (5), 2706-2710.
- (34) de Maat-Gersdorf, I. Spectroscopic analysis of erbium-doped silicon and ytterbium doped indium phosphide. University of Amsterdam, 2001.
- (35) Wyart, J.-F.; Tchang-Brillet, W.-Ü. L.; Spector, N.; Palmeri, P.; Quinet, P.; Biémont, E. Extended Analysis of the Spectrum of Triply-ionized Ytterbium (Yb IV) and Transition Probabilities. *Phys. Scripta* **2001**, *63* (2), 113-121.
- (36) De Siena, M. C.; Creutz, S. E.; Regan, A.; Malinowski, P.; Jiang, Q.; Kluherz, K. T.; Zhu, G.; Lin, Z.; De Yoreo, J. J.; Xu, X.; Chu, J.-H.; Gamelin, D. R. Two-Dimensional van der Waals Nanoplatelets with Robust Ferromagnetism. *Nano Lett.* **2020**, *20* (3), 2100-2106.